The Astronomical Journal, 132:2268–2288, 2006 December

SPITZER SURVEY OF THE LARGE MAGELLANIC CLOUD: SURVEYING THE AGENTS OF A GALAXY'S EVOLUTION (SAGE). I. OVERVIEW AND INITIAL RESULTS

Margaret Meixner,[1] Karl D. Gordon,[2] Remy Indebetouw,[3] Joseph L. Hora,[4] Barbara Whitney,[5] Robert Blum,[6] William Reach,[7] Jean-Philippe Bernard,[8] Marilyn Meade,[9] Brian Babler,[9] Charles W. Engelbracht,[2] Bi-Qing For,[2] Karl Misselt,[2] Uma Vijh,[1] Claus Leitherer,[1] Martin Cohen,[10] Ed B. Churchwell,[10] Francois Boulanger,[11] Jay A. Frogel,[12] Yasuo Fukui,[13] Jay Gallagher,[9] Varoujan Gorjian,[14] Jason Harris,[2] Douglas Kelly,[2] Akiko Kawamura,[13] SoYoung Kim,[15] William B. Latter,[7] Suzanne Madden,[16] Ciska Markwick-Kemper,[3] Akira Mizuno,[13] Norikazu Mizuno,[13] Jeremy Mould,[17] Antonella Nota,[1] M.S. Oey,[18] Knut Olsen,[2] Toshikazu Onishi,[13] Roberta Paladini,[7] Nino Panagia,[1] Pablo Perez-Gonzalez,[2] Hiroshi Shibai,[13] Shuji Sato,[13] Linda Smith,[1,19] Lister Staveley-Smith,[20] A. G. G. M. Tielens,[21] Toshiya Ueta,[22] Schuyler Van Dyk,[7] Kevin Volk,[23] Michael Werner,[24] and Dennis Zaritsky[2]

Received 2006 February 10; accepted 2006 June 9

ABSTRACT

We are performing a uniform and unbiased imaging survey of the Large Magellanic Cloud (LMC; $\sim 7^\circ \times 7^\circ$) using the IRAC (3.6, 4.5, 5.8, and 8 μm) and MIPS (24, 70, and 160 μm) instruments on board the *Spitzer Space Telescope* in the Surveying the Agents of a Galaxy's Evolution (SAGE) survey, these agents being the interstellar medium (ISM) and stars in the LMC. This paper provides an overview of the SAGE Legacy project, including observing strategy, data processing, and initial results. Three key science goals determined the coverage and depth of the survey. The detection of diffuse ISM with column densities $>1.2 \times 10^{21}$ H cm^{-2} permits detailed studies of dust processes in the ISM. SAGE's point-source sensitivity enables a complete census of newly formed stars with masses $>3\ M_\odot$ that will determine the current star formation rate in the LMC. SAGE's detection of evolved stars with mass-loss rates $>1 \times 10^{-8}\ M_\odot$ yr^{-1} will quantify the rate at which evolved stars inject mass into the ISM of the LMC. The observing strategy includes two epochs in 2005, separated by 3 months, that both mitigate instrumental artifacts and constrain source variability. The SAGE data are nonproprietary. The data processing includes IRAC and MIPS pipelines and a database for mining the point-source catalogs, which will be released to the community in support of *Spitzer* proposal cycles 4 and 5. We present initial results on the epoch 1 data for a region near N79 and N83. The MIPS 70 and 160 μm images of the diffuse dust emission of the N79/N83 region reveal a similar distribution to the gas emissions, especially the H I 21 cm emission. The measured point-source sensitivity for the epoch 1 data is consistent with expectations for the survey. The point-source counts are highest for the IRAC 3.6 μm band and decrease dramatically toward longer wavelengths,

[1] Space Telescope Science Institute, 3700 San Martin Drive, Baltimore, MD 21218; meixner@stsci.edu, leitherer@stsci.edu, vijh@stsci.edu, nota@stsci.edu, panagia@stsci.edu.
[2] Steward Observatory, University of Arizona, 933 North Cherry Avenue, Tucson, AZ 85721; kgordon@as.arizona.edu, cengelbracht@as.arizona.edu, biqing@email.arizona.edu, kmisselt@as.arizona.edu, pgperez@as.arizona.edu, jharris@as.arizona.edu, dkelly@as.arizona.edu, dennis@fishingholes.as.arizona.edu.
[3] Department of Astronomy, University of Virginia, P.O. Box 3818, Charlottesville, VA 22903-0818; remy@virginia.edu, fk2n@virginia.edu.
[4] Harvard-Smithsonian Center for Astrophysics, 60 Garden Street, MS 65, Cambridge, MA 02138-1516; jhora@cfa.harvard.edu.
[5] Space Science Institute, 4750 Walnut Street, Suite 205, Boulder, CO 80301; bwhitney@spacescience.org.
[6] Cerro Tololo Inter-American Observatory, Casilla 603, La Serena, Chile; rblum@ctio.noao.edu, kolsen@ctio.noao.edu.
[7] *Spitzer* Science Center, Jet Propulsion Laboratory, California Institute of Technology, MS 220-6, Pasadena, CA 91125; reach@ipac.caltech.edu, vandyk@ipac.caltech.edu, paladini@ipac.caltech.edu.
[8] Direction de la Recherche, Centre d'Etude Spatiale des Rayonnements, 18 Avenue Edouard Belin, Toulouse Cedex F-31055, France; jean-philippe.bernard@cesr.fr.
[9] Department of Astronomy, University of Wisconsin, Madison, 475 North Charter Street, Madison, WI 53706-1582; meade@sal.wisc.edu, brian@sal.wisc.edu, ebc@astro.wisc.edu, jsg@astro.wisc.edu.
[10] Radio Astronomy Laboratory, University of California at Berkeley, 601 Campbell Hall, Berkeley, CA 94720-3411; mcohen@astro.berkeley.edu.
[11] Institut d'Astrophysique de Paris, CNRS UPR 341, 98bis, Boulevard Arago, Paris F-75014, France; francois.boulanger@ias.u-psud.fr.
[12] Association of Universities for Research in Astronomy, Inc., Suite 350, 1200 New York Avenue NW, Washington, DC 20005; jfrogel@aura-astronomy.org.
[13] Department of Astrophysics, Nagoya University, Chikusa-Ku, Nagoya 464-01, Japan; fukui@a.phys.nagoya-u.ac.jp, kawamura@a.phys.nagoya-u.ac.jp, mizuno@a.phys.nagoya-u.ac.jp, norikazu@a.phys.nagoya, ohnishi@a.phys.nagoya-u.ac.jp, shibai@nagoya-u.jp, ssato@z.phys.nagoya-u.ac.jp.
[14] Jet Propulsion Laboratory, 4800 Oak Grove Boulevard, MS 169-327, Pasadena, CA 91109; varoujan.gorjian@jpl.nasa.gov.
[15] Department of Physics and Astronomy, Johns Hopkins University, Homewood Campus, Baltimore, MD 21218; sykim@pha.jhu.edu.
[16] Service d'Astrophysique, Commissart à L'Energie Atomique de Saclay, 91191 Gif-sur-Yvette, France; smadden@cea.fr.
[17] National Optical Astronomy Observatory, 950 North Cherry Avenue, Tucson, AZ 85726-6732; jmould@noao.edu.
[18] Department of Astronomy, University of Michigan, 830 Dennison Building, Ann Arbor, MI 48109-1042; msoey@umich.edu.
[19] Department of Physics and Astronomy, University College London, Gower Street, London WC1E 6BT, UK; ljs@zuaxp0.star.ucl.ac.uk.
[20] Commonwealth Science and Industrial Research Organization, Head Office, GPO Box 4908, Melbourne, VIC 3001, Australia; lister.staveley-smith@csiro.au.
[21] NASA Ames Research Center, SOFIA Office, MS 211-3, Moffett Field, CA 94035; tielens@astro.rug.nl.
[22] Current address: Department of Physics and Astronomy, University of Denver, Denver, CO 80208; and NASA Ames Research Center, URSA SOFIA Office, MS 211-3, Moffett Field, CA 94035; tueta@mail.sofia.usra.edu.
[23] Gemini Observatory, Northern Operations Center, 670 North A'ohuku Place, Hilo, HI 96720; kvolk@gemini.edu.
[24] Jet Propulsion Laboratory, 4800 Oak Grove Boulevard, MS 264-767, Pasadena, CA 91109; mwerner@sirtfweb.jpl.nasa.gov.

consistent with the fact that stars dominate the point-source catalogs and the dusty objects detected at the longer wavelengths are rare in comparison. The SAGE epoch 1 point-source catalog has $\sim 4 \times 10^6$ sources, and more are anticipated when the epoch 1 and 2 data are combined. Using Milky Way (MW) templates as a guide, we adopt a simplified point-source classification to identify three candidate groups—stars without dust, dusty evolved stars, and young stellar objects—that offer a starting point for this work. We outline a strategy for identifying foreground MW stars, which may comprise as much as 18% of the source list, and background galaxies, which may comprise ~12% of the source list.

Key words: dust, extinction — ISM: general — Magellanic Clouds — stars: AGB and post-AGB — stars: formation — stars: mass loss — supergiants — surveys

Online material: color figures, machine-readable table

1. INTRODUCTION

The interstellar medium (ISM) plays a central role in the evolution of galaxies as the birth site of new stars and the repository of old stellar ejecta. The formation of new stars slowly consumes the ISM, locking it up for millions to billions of years. As these stars age, the winds from low-mass, asymptotic giant branch (AGB) stars, high-mass, red supergiants (RSGs), and supernova explosions inject the nucleosynthetic products of stellar interiors into the ISM, progressively increasing its metallicity. This constant recycling and the associated enrichment drive the evolution of a galaxy's baryonic matter and change its emission characteristics. To understand this recycling, we have to study the physical processes of the ISM, the formation of new stars, the injection of mass by evolved stars, and their interrelationship on a galaxy-wide scale.

Among the nearby galaxies, the Large Magellanic Cloud (LMC) is the best astrophysical laboratory for studies of the life cycle of baryonic matter, because its proximity (~50 kpc; Feast 1999) and its favorable viewing angle (35°; van der Marel & Cioni 2001) permit studies of the resolved stellar populations and ISM clouds. The ISM in the Milky Way (MW) and in the Small Magellanic Cloud (SMC) is confused in infrared (IR) images due to crowding along the line of sight. In contrast, all LMC features are at approximately the same distance from the Sun, and there is typically only one substantial cloud along a given line of sight, so their relative masses and luminosities are directly measurable. The LMC also offers a rare glimpse into the physical processes in an environment with spatially varying subsolar metallicity ($Z \sim 0.3-0.5\ Z_\odot$; Westerlund 1997, p. 234) that is similar to the mean metallicity of the ISM during the epoch of peak star formation in the universe (redshift of ~1.5; Madau et al. 1996; Pei et al. 1999). The dust-to-gas mass ratio has real spatial variations and is ~2–4 times lower than the value for the solar neighborhood (Gordon et al. 2003), resulting in substantially higher ambient UV fields than in the solar neighborhood. The LMC has been surveyed with many instruments, revealing structures on all scales and a global asymmetry that varies with wavelength (Fig. 1). The ISM gas that fuels star formation (Fukui et al. 1999; Mizuno et al. 2001; Y. Fukui et al. 2006, in preparation; Staveley-Smith et al. 2003; Kim et al. 2003), the stellar components that trace the history of star formation (Zaritsky et al. 2004; Van Dyk et al. 1999; Nikolaev & Weinberg 2000; Holtzman et al. 1999; Olsen 1999; J. Harris & D. Zaritsky 2006, in preparation), and the dust (Schwering 1989; Egan et al. 2001; Zaritsky et al. 2004) have all been mapped in the LMC (Fig. 1). From the perspective of galaxy evolution, the LMC is uniquely suited to study how the agents of evolution, the ISM and stars, interact as a whole in a galaxy that has undergone tidal interactions with other galaxies, the MW and the SMC (Zaritsky & Harris 2004; Harris & Zaritsky 2004; Bekki & Chiba 2005).

The study of the life cycle of galaxies has been hampered by the association of dust with the key objects driving this galactic evolution—evolved stars and protostars—and the associated extinction of the light of these objects. However, the absorbed stellar light is reradiated by the dust in the IR, and this emission provides an effective tracer of stellar mass loss, star formation, and the ISM in general. The launch of the *Spitzer Space Telescope* (Werner et al. 2004) with its sensitive detector arrays provides the necessary IR tools for the Surveying the Agents of a Galaxy's Evolution (SAGE) survey, which surveys the ISM and stars and thereby traces the life cycle of baryonic matter. We are conducting a uniform $\sim 7^\circ \times 7^\circ$ survey of the LMC in all the IRAC (3.6, 4.5, 5.8, and 8.0 μm) and MIPS (24, 70, and 160 μm) bands (Fig. 1). The SAGE project builds on previous IR surveys of the LMC. The all-sky IR survey by *IRAS* included $8\overset{\circ}{.}5 \times 8\overset{\circ}{.}5$ of pointed observations of the LMC imaged at 12, 25, 60, and 100 μm (Fig. 1) with an angular resolution of ~1′ and resulted in a point-source list of 1823 objects (Schwering 1989). The $10^\circ \times 10^\circ$ *Midcourse Space Experiment* (*MSX*) imaging survey of the LMC at 8.3 μm with an angular resolution of ~20″ provided a source list of 1806 objects with more precise positions than *IRAS*, enabling cross-correlation with ground-based near-IR surveys such as the Two Micron All Sky Survey (2MASS; Egan et al. 2001). Both of these previous far-IR surveys revealed the most luminous dusty inhabitants of the LMC—supergiants, AGB stars, H II regions, and planetary nebulae—but lacked the angular resolution and corresponding point-source sensitivity to detect the more populous, less luminous sources. On the other hand, the ground-based near-IR surveys of the LMC based on 2MASS at J (1.25 μm), H (1.65 μm), and K_s (2.15 μm) (Nikolaev & Weinberg 2000) and DENIS at I (0.8 μm), J (1.25 μm), H (1.65 μm), and K_s (2.15 μm) (Cioni et al. 2000) revealed ~820,000 and ~1.3 million sources, respectively, consisting of red giants, AGB stars, and supergiants. These near-IR surveys detected many more sources than the far-IR surveys because of their better angular resolution and because their wave bands are more sensitive to stellar photospheres, which are more numerous than the dust-enshrouded objects. One of the purposes of SAGE is to push this IR survey work to the fainter and more numerous dusty sources in the LMC.

The remainder of this paper is organized as follows. Section 2 describes SAGE, including the science drivers and observing strategy. Section 3 describes the data-processing approach and the Legacy aspects of SAGE. Section 4 takes a preliminary look at some of the initially processed SAGE data for a region surrounding N83 and N79, near the western end of the bar. Section 5 summarizes the paper.

2. SAGE OBSERVING PROGRAM

SAGE is a uniform and unbiased $\sim 7^\circ \times 7^\circ$ survey of the LMC in all the IRAC (3.6, 4.5, 5.8, and 8 μm) and MIPS (24, 70, and 160 μm) bands using 508 total hours (291 IRAC, 217 MIPS) of

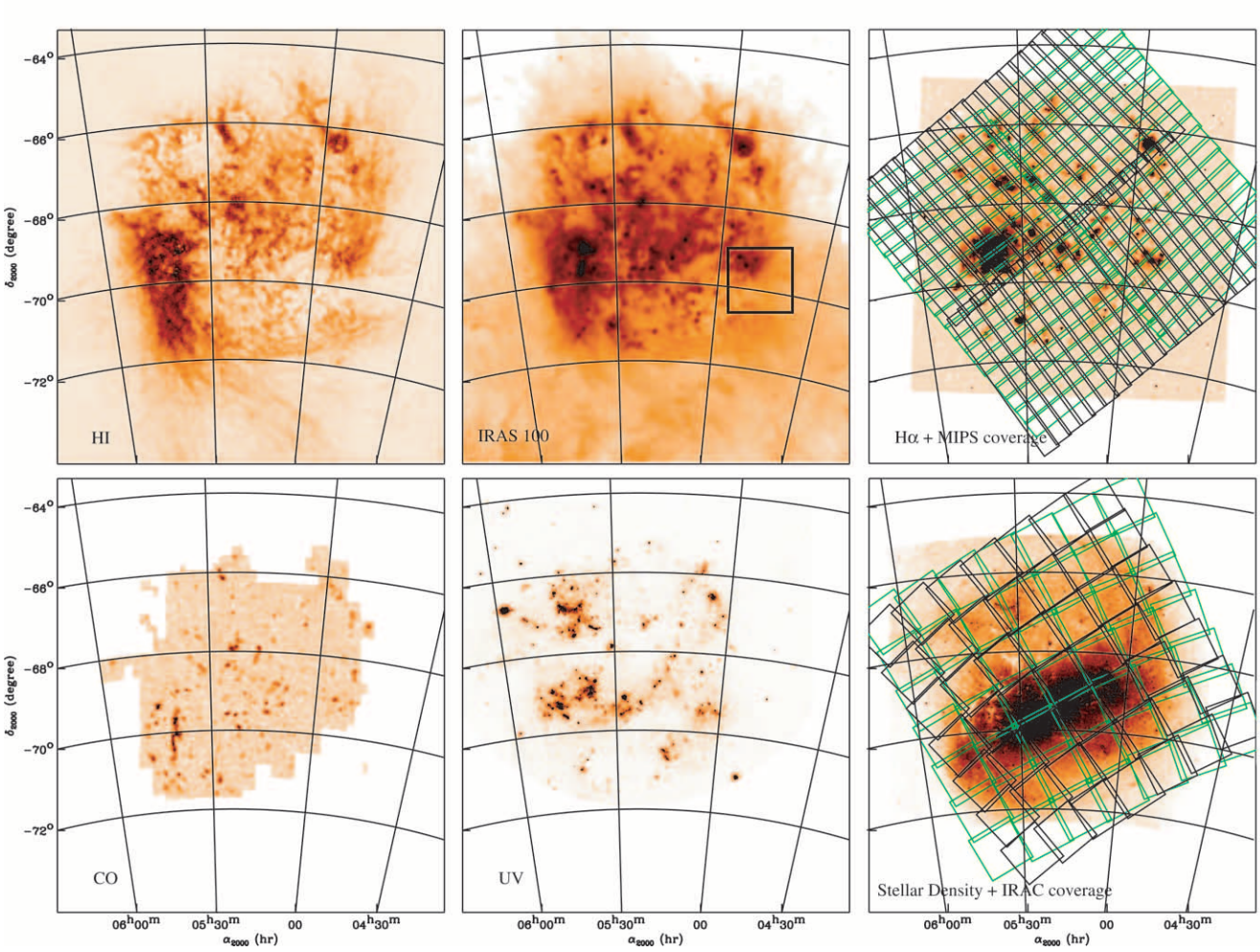

FIG. 1.—Examples of the many existing LMC surveys: H I (Staveley-Smith et al. 2003; Kim et al. 2003), CO (Fukui et al. 2001; Y. Fukui et al. 2006, in preparation), *IRAS* 100 μm, Hα (Gaustad et al. 2001) with the SAGE MIPS coverage overlaid, UV (Smith et al. 1987), and stellar density (Zaritsky et al. 2004) with the SAGE IRAC coverage overlaid. The SAGE survey maps the LMC twice. Epoch 1 coverage is outlined in green, and epoch 2 coverage is outlined in black. The location of the N79/N83 region, discussed in § 4, is outlined by the square box in the *IRAS* 100 μm image.

TABLE 1

PRINCIPAL CHARACTERISTICS OF THE SAGE SURVEY, *Spitzer* PROGRAM ID 20203

Characteristic	IRAC Value	MIPS Value
Nominal center point[a]	$\alpha = 05\ 18\ 48$, $\delta = -68\ 34\ 12$	$\alpha = 05\ 18\ 48$, $\delta = -68\ 34\ 12$
Survey area (deg)	7.1×7.1	7.8×7.8
AOR size	$1\overset{\circ}{.}1 \times 1\overset{\circ}{.}1$	$25' \times 4^{\circ}$
AOR grid size	7×7	19×2
Total time (hr)	290.65	216.84
λ (μm)	3.6, 4.5, 5.8, and 8	24, 70, and 160
Pixel size at λ (arcsec)	1.2, 1.2, 1.2, and 1.2	2.5, 9.8, and 15.9
Angular resolution at λ (arcsec)	1.7, 1.7, 1.9, and 2	6, 18, and 40
Exposure time per pixel at λ (s)	43, 43, 43, and 43	60, 30, and 6
Predicted point-source sensitivity, 5 σ at λ (mJy)	0.0051, 0.0072, 0.041, and 0.044	0.5, 30, and 275
Predicted point-source sensitivity, 5 σ at λ (mag)	19.3, 18.5, 16.1, and 15.4	10.4, 3.5, and -0.6
Saturation limits at λ (Jy)	1.1, 1.1, 7.4, and 4.0	4.1, 23, and 3
Saturation limits at λ (mag)	6, 5.5, 3.0, and 3.0	0.60, -3.7, and -3.2
Surface brightness limits 5 σ at λ (MJy sr^{-1})	. . . , . . . , 0.5, and 1	1, 5, and 10
Epoch 1	2005 Jul 15–26	2005 Jul 27–Aug 3
Epoch 2	2005 Oct 26–Nov 2	2005 Nov 2–9

[a] Units of right ascension are hours, minutes, and seconds, and units of declination are degrees, arcminutes, and arcseconds.

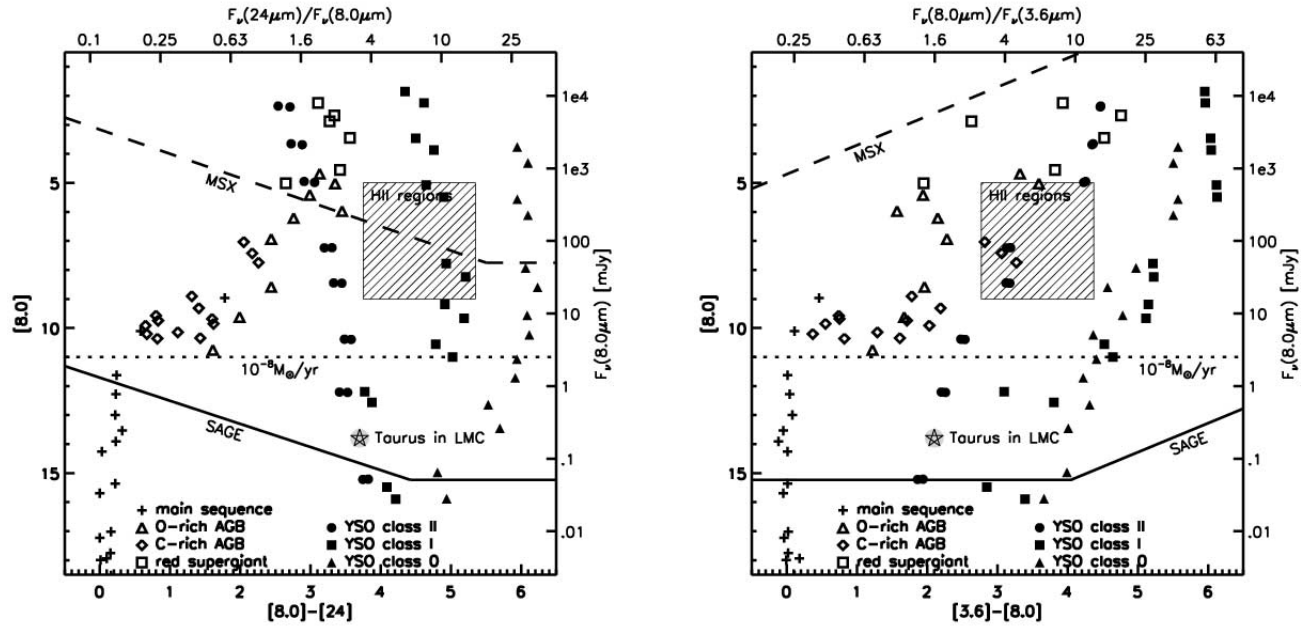

FIG. 2.—*Spitzer* CMDs showing the discovery space for SAGE. Square brackets denote the brightness in Vega magnitudes at the wavelength enclosed in the brackets. For example, [8.0] means the Vega magnitude at 8.0 μm. The symbols identify populations of key sources throughout the LMC: YSOs (1–30 $M_{\odot}$), H II regions, Taurus-like clusters, O-rich and C-rich AGB stars, RSGs, and main-sequence O stars. Symbols, defined in the figure, represent the template/model photometry of Cohen (1993) and Whitney et al. (2004). SAGE's sensitivity limit (*solid line*) falls 1000 times below the *MSX* limit (*dashed line*) and the lower limit to AGB mass loss, $>10^{-8}\ M_{\odot}\ \mathrm{yr}^{-1}$ (*dotted line*). The circle with a star represents a subregion of Taurus containing ~12 stars, placed at the distance of the LMC. [*See the electronic edition of the Journal for a color version of this figure.*]

Spitzer. The principal characteristics of SAGE are summarized in Table 1. The spatial coverage shown in Figure 1 extends beyond the IR edge of the LMC's star formation activity and provides adequate background for calibration and measurement of non-LMC populations. The point-source sensitivity estimates for the SAGE survey, listed in Table 1, improve on previous IR surveys with *MSX* (Egan et al. 2001) and *IRAS* (Schwering 1989) by a factor of ~1000 and have better wavelength coverage. This sensitivity improvement is due to the more sensitive detectors and improved angular resolution. The angular resolution is ~2″ (0.5 pc at the distance to the LMC) in the IRAC bands and 6″ (1.5 pc), 18″ (4.5 pc), and 40″ (10 pc) in the MIPS 24, 70, and 160 μm bands, respectively. The IRAC 8 μm and MIPS 24 μm images have a 100 times better areal resolution, which is proportional to angular resolution squared, than the *MSX* (8 μm) and *IRAS* 25 μm surveys. The MIPS 70 μm band has an 11 times better areal resolution compared to the *IRAS* 60 μm survey. The MIPS 160 μm band has a 2.3 times better areal resolution compared to the *IRAS* 100 μm survey. Below we describe the science drivers for the survey's characteristics and the observing strategy implemented to meet these goals.

2.1. *Science Drivers*

SAGE is designed to detect the population of IR point sources down to the confusion limit imposed by *Spitzer*'s spatial resolution and to map, with high signal-to-noise ratio (S/N), the dust emission from diffuse and molecular clouds, photodissociation regions (PDRs), and H II regions. SAGE's coverage and sensitivity limits are driven by the science goals of the SAGE survey in three areas: star formation, evolved stars, and ISM.

2.1.1. *Star Formation*

Star formation in the LMC appears to be a stochastic process, in which stars form in clumps, clusters, and supershells (e.g., Panagia et al. 2000; Walborn et al. 1999). Star formation may be self-propagating through the energetic feedback of stellar winds and supernovae (e.g., Oey & Massey 1995; Efremov & Elmegreen 1998), but this stellar feedback also acts to eventually squelch star formation by dissipating the local ISM (Yamaguchi et al. 2001; Israel et al. 2003). The CO survey of the LMC (Fukui et al. 2001; Y. Fukui et al. 2006, in preparation) has uncovered 272 giant molecular clouds (GMCs) with masses and radii similar to MW GMCs. Current optical and near-IR observations reveal that one-third of the LMC GMCs are forming compact young massive star clusters, e.g., R136 in 30 Dor, while an equally large fraction exhibit no massive star formation (Blitz et al. 2006; Y. Fukui et al. 2006, in preparation). This contrast in star formation activity may indicate a phase of deeply embedded or lower mass star formation in the latter. To date, searches for IR young stellar objects (YSOs) have been targeted near current star formation. The first detected YSO (or protostar), N159-P1 (Gatley et al. 1982), and its surroundings have been the subject of several follow-ups, the most recent of which is a detailed *Spitzer* study of the region by Jones et al. (2005). Studies of the Henize 206 region by Gorjian et al. (2004) and the LMC superbubble, N51D, by Chu et al. (2005) show the potential of *Spitzer* imaging in discovering and characterizing new YSOs in the LMC. In order to obtain an unbiased and complete census of star formation throughout the LMC, SAGE is required to be sensitive to all star formation activity from the massive star formation traced by H II regions to the lower mass star formation traced by Taurus-like complexes (Fig. 2). Variability of some YSOs, e.g., FU Ori systems, may be detectable in the two epochs of photometry.

2.1.2. *Evolved Stars*

High mass loss during the AGB and RSG phases leads to the formation of circumstellar envelopes that are observable via their dust emission in all IRAC and MIPS bands. Stellar mass loss can drive the late stages of stellar evolution, yet the mechanism for mass loss remains poorly understood. Moreover, this mass loss is

a dominant source of dust and gas return to the ISM. However, present estimates disagree on the relative contributions from these different stellar classes to the injected mass budget of a galaxy (Tielens 2001). Measuring the mass-loss rates of the entire population of evolved stars will help constrain stellar evolution modeling and the total returned mass to the LMC's ISM.

Studies based on previous IR surveys have delved into these evolved star topics. The *IRAS* catalog was used by Loup et al. (1997) to select 198 mass-losing AGB stars. Trams et al. (1999) followed up on this *IRAS*-selected sample with the *Infrared Space Observatory* (*ISO*), deriving colors and chemical compositions. Van Loon et al. (1999) derived mass-loss rates for these *ISO* sources, finding a trend of increasing mass-loss rate with luminosity. However, this *IRAS*-selected sample was limited to only the most luminous AGB stars ($L > 10^4\ L_\odot$) with high mass-loss rates ($5 \times 10^{-6}\ M_\odot\ \mathrm{yr}^{-1}$). Using ISOCAM, Loup et al. (1999) detected ~300 mass-losing AGB stars at significantly lower luminosities (~10 mag at 8 μm) and mass-loss rates but over a limited area, 0.5 deg^2 in the LMC bar.

In order to obtain a complete picture of mass loss among the LMC's evolved stars, each epoch of SAGE photometry is required to be sensitive to all evolved stars with mass loss that produces dust at significant rates; i.e., mass-loss rates $>10^{-8}\ M_\odot\ \mathrm{yr}^{-1}$ (Fig. 2). In addition, we will be able to constrain the variability of evolved stars by comparing photometry derived by analyzing the two epochs separately. The 3 month separation of the epochs is well-suited to detecting evolved star variability, which typically has a period of approximately 1 yr (Wood et al. 1999).

2.1.3. *ISM*

The dust properties in the different phases of the ISM provide insight into the evolution of the dust between phases, as well as the relationship of the dust components to stellar sources of UV radiation and kinetic energy. UV extinction measurements have indicated that the dust properties in the LMC vary spatially (Gordon et al. 2003). Most of the dust mass is in the largest grains and is traced by far-IR dust emission, such as in the MIPS 70–160 μm images. Comparison of these images with the H I (Staveley-Smith et al. 2003; Kim et al. 2003) and CO data (Fukui et al. 1999) can be used to map out the dust-to-gas ratio across the LMC to search for variations. In addition to the amount of dust, the grain size distribution can be measured using the color ratios, where IRAC 3.6, 5.8, and 8 μm trace polycyclic aromatic hydrocarbon (PAH) emission, MIPS 24 μm traces small grains, and the MIPS 70 + 160 μm traces larger grains. In particular, variations in the properties of the smallest grains, as traced by PAH emission, are of fundamental importance to the thermodynamics of the ISM because small grains are very efficient in heating the gas through the photoelectric effect (Bakes & Tielens 1994). The analysis of the *IRAS* data on the LMC indicates a lower 12 μm diffuse emission in comparison to the MW and suggests a deficit of very small dust grains, possibly due to the intense UV radiation of the LMC (Schwering 1989). SAGE's complete IRAC mapping of the lower metallicity LMC will yield high-resolution insight into recent work on the paucity of PAH emission in low-metallicity galaxies (Madden 2000, 2006; Houck et al. 2004; Engelbracht et al. 2005; Galliano et al. 2005; Dale et al. 2005; Wu et al. 2006; O'Halloran et al. 2006). The absence of PAH and small grains will have a profound influence on the gas heating and the existence of cold and warm phases in the ISM (Wolfire et al. 1995). In order to carry out these ISM studies, SAGE must be sensitive to diffuse dust emission corresponding to column densities $>1.2 \times 10^{21}$ H cm^{-2} ($A_V = 0.2$ mag). Residual images, which are images with the point sources subtracted and smoothed to improve the S/Ns, will be used for the studies of the diffuse ISM. The angular resolution achieved by SAGE is sufficient to separate the stars from the ISM and to distinguish the major cloud populations: H II regions, photodissociation regions, molecular clouds, atomic clouds, and diffuse medium.

2.2. *Observing Strategy*

2.2.1. *Mapping Strategy*

To achieve the science and sensitivity goals, the LMC was mapped at two different epochs separated by 3 months, as detailed in Table 1. The region is many times too large to map with one Astronomical Observing Request (AOR), so the survey area was divided into smaller regions that could be efficiently planned and scheduled. For IRAC, the area was divided into 7×7 tiles of $1\overset{\circ}{.}1 \times 1\overset{\circ}{.}1$ each, composed of 14×28 pointings of high dynamic range (HDR) 0.6 and 12 s frames with half-array steps with a total duration of 10,687 s per AOR. The HDR 0.6 and 12 s frames have corresponding exposure times of 0.4 and 10.4 s. We refer to these frames as the 0.6 and 12 s frames throughout the paper. Mapping steps were done instead of dithers to minimize the time required to cover the desired area. This IRAC mapping technique has been used with good success on the Galactic Legacy Infrared Mid-Plane Survey Extraordinaire (GLIMPSE) *Spitzer* project (Benjamin et al. 2003). Each position in the SAGE IRAC survey has at least four frames of coverage, resulting in an exposure time per pixel of at least 43.2 s in all IRAC bands for the complete survey and a quarter of that, 11 s, for the single-frame photometry of each epoch. The LMC was mapped in 145.5 hr per epoch, for a total of 291 hr of IRAC observing time.

For MIPS, the approximately $7\overset{\circ}{.}8 \times 7\overset{\circ}{.}8$ region centered on the LMC was covered by 38 AORs, each covering approximately $25'' \times 4^\circ$. A MIPS AOR consists of 10 4° fast-scan legs with half-array cross-scan steps, with a duration of 2.85 hr. The LMC is mapped with a 19×2 grid of these AORs, taking 108.5 hr per epoch, or a total of 217 hr. Tight sequential constraints relative to the roll angle rate of change have been invoked so that neighboring long strips have sufficient overlap. We have carefully designed our MIPS strategy to allow for off-source measurements in *every* scan leg, which allows for accurate self-calibration of the instrumental effects. While the MIPS fast-scan mode does not achieve full coverage at 160 μm, the combined epoch 1 and 2 map has a good basket-weave pattern with small gaps less than a pixel in size. The well-sampled 160 μm point-spread function (PSF; ~3 pixels per FWHM) means that interpolation can be used to fill the gaps. Each position in the SAGE MIPS survey has 20, 10, and ~3 frames of coverage at 24, 70, and 160 μm, respectively. The exposure times per pixel are 60, 30, and 6 s at 24, 70, and 160 μm, respectively, for the complete survey and half these values for each epoch's photometry.

The mapping strategy maximizes observing efficiency while minimizing artifacts that compromise data quality and limit the scientific interpretation. The IRAC and MIPS artifacts fall into two classes: random artifacts (e.g., cosmic rays and bad pixels) and systematic artifacts that are tied to pixel location and usually systematically affect rows/columns. The random artifacts are easily removed, since our mapping strategy provides four images at each location (two overlapping images per epoch). The 3 month time baseline between epochs is ideal for the removal of the systematic artifacts, because it provides a 90° roll angle in the orientation of the detectors, which optimally removes the "striping" artifacts in MIPS and IRAC image data. In addition, these two

TABLE 2
EPOCH 1: INITIAL RESULTS FOR POINT-SOURCE SENSITIVITIES AND SOURCE COUNTS

λ (1)	Epoch 1 Limiting Flux (mJy) (2)	Epoch 1 Limiting Magnitude (3)	No. of Sources Detected in N79/N83 Field (4)	Lower Limit to No. of Sources Predicted in the Epoch 1 SAGE Survey (5)	No. of Sources in the SAGE IRAC Epoch 1 Point-Source Catalog (6)
3.6 μm	0.0127[a]	18.348	119333	2.92×10^6	3.94×10^6
4.5 μm	0.01839[a]	17.474	59129	1.45×10^6	2.00×10^6
5.8 μm	0.1001[a]	15.164	13292	3.26×10^5	4.61×10^5
8.0 μm	0.1288[b]	14.226	7763	1.90×10^5	2.60×10^5
24 μm	0.211[c]	11.34	5115	1.25×10^5	...
70 μm	23.9[c]	3.8	1024	2.50×10^4	...
160 μm	142[c]	0.12	46	1130	...
3.6 and 4.5 μm	...	...	56599	1.39×10^6	1.90×10^6
All IRAC	...	...	6737	1.65×10^5	2.26×10^5
IRAC+2MASS *J*, *H*, and *K*	...	...	6422	1.57×10^5	2.15×10^5
IRAC+24	...	...	627	1.57×10^4	...
3.6, 8.0, and 24 μm	...	...	1175	2.88×10^4	...

[a] 6 σ.
[b] 10 σ.
[c] 3 σ.

epochs are useful constraints of source variability expected for evolved stars and some YSOs.

2.2.2. *Point-Source Sensitivities*

The point-source sensitivity estimates for the survey listed in column (1) of Table 2 are a priori estimates derived from the *Spitzer* IRAC and MIPS exposure time calculators, SENS-PET, for isolated point sources for a medium background. Figure 2 shows example color-magnitude diagrams (CMDs) for the LMC that illustrate how the sensitivity limits meet the requirements to study the two populations of greatest interest: forming stars and evolved stars. An IRAC sensitivity as faint as $[8.0] = 15$ mag[25] (0.044 mJy) allows the measurement of YSOs down to a few solar masses (the limit depends on the age, as younger YSOs of a given mass are more luminous) and of Taurus-like clusters in the LMC (Fig. 2). An IRAC sensitivity as faint as $[8.0] \sim 11$ mag (1.7 mJy) ensures that all dusty evolved stars with mass-loss rates $>10^{-8}\ M_\odot\ \mathrm{yr}^{-1}$ are detected as inferred from *ISO* observations by Glass et al. (1999) and Alard et al. (2001) on the Galactic bulge and by Ramdani & Jorissen (2001) on the low-metallicity globular cluster 47 Tuc.

2.2.3. *Surface Brightness Sensitivities*

The SAGE surface brightness sensitivity to the diffuse emission in the LMC is anticipated to be $\sim$0.5, 1, 1, 5, and 10 MJy sr^{-1} at 5.8, 8.0, 24, 70, and 160 μm, respectively, with a resulting S/N of $\sim$5 per pixel based on similar observations of other nearby galaxies (e.g., M81; Gordon et al. 2004; Willner et al. 2004). The removal of artifacts is particularly important for achieving the surface brightness goal. From these diffuse emission sensitivity limits in the MIPS and IRAC 5.8 and 8 μm bands, we estimate a minimum detectable column density of $\sim 1.2 \times 10^{21}$ H cm^{-2} ($A_V = 0.2$ mag) by assuming a solar neighborhood spectral energy distribution for the diffuse dust emission (Desert et al. 1990) and the LMC gas-to-dust ratio. The IRAC 3.6 and 4.5 μm bands also detect this same column density when their angular resolution is degraded to the 160 μm band.

[25] Square brackets denote the brightness in Vega magnitudes at the wavelength enclosed in the brackets. For example, [8.0] means the Vega magnitude at 8.0 μm.

3. DATA-PROCESSING APPROACH

The full LMC mosaics of the IRAC and MIPS (Figs. 3 and 4) data show the coverage of the SAGE survey with these two instruments over the two epochs. While the analysis of these LMC images will be the subject of future papers, we comment briefly on them here in the context of data processing. The LMC three-color IRAC (Fig. 3*a*) and three-color IRAC/MIPS24 (Fig. 4) images reveal the stellar component to be dominated by the bar at 3.6 and 4.5 μm and visually demonstrate the millions of point sources that are extracted for the SAGE catalogs. The wispy, highly sculpted dust emission of the LMC's ISM appears at 8 and 24 μm in the three-color IRAC and IRAC/MIPS images (Figs. 3*a* and 4) and at 24, 70, and 160 μm in the three-color MIPS image (Fig. 3*b*). The investigation of the ISM relies on well-calibrated images on both small and large scales.

In the spirit of previous *Spitzer* Legacy projects, the SAGE data are nonproprietary. In addition, a uniform Legacy data product, consisting of point-source lists and mosaicked images, will be produced by the SAGE team for the community. In support of *Spitzer* proposal cycle 4, point-source catalogs for the epoch 1 data will be made available through the *Spitzer* Science Center (SSC) well in advance of the deadline. For *Spitzer* proposal cycle 5, point-source catalogs and refined mosaicked images of $1^\circ \times 1^\circ$ tiles will be made available through the SSC. For announcement of releases, see the Web sites of the SSC[26] and SAGE.[27] The SAGE IRAC and MIPS pipelines are processing the SAGE epoch 1 and epoch 2 data separately in order to obtain the source fluxes at different times and will then stack the image data into a mosaicked image and derive final, deeper source lists from these mosaicked images. Here in § 3 we describe the IRAC and MIPS processing for epoch 1 data.

3.1. *IRAC Pipeline*

The Wisconsin pipeline produces two data products from the flux-calibrated IRAC (Reach et al. 2005) data provided by the SSC: point-source catalogs and mosaic images. The data presented in this paper were processed with the SSC pipeline version S12.4.0. The Wisconsin pipeline was originally developed

[26] See http://ssc.spitzer.caltech.edu.
[27] See http://sage.stsci.edu.

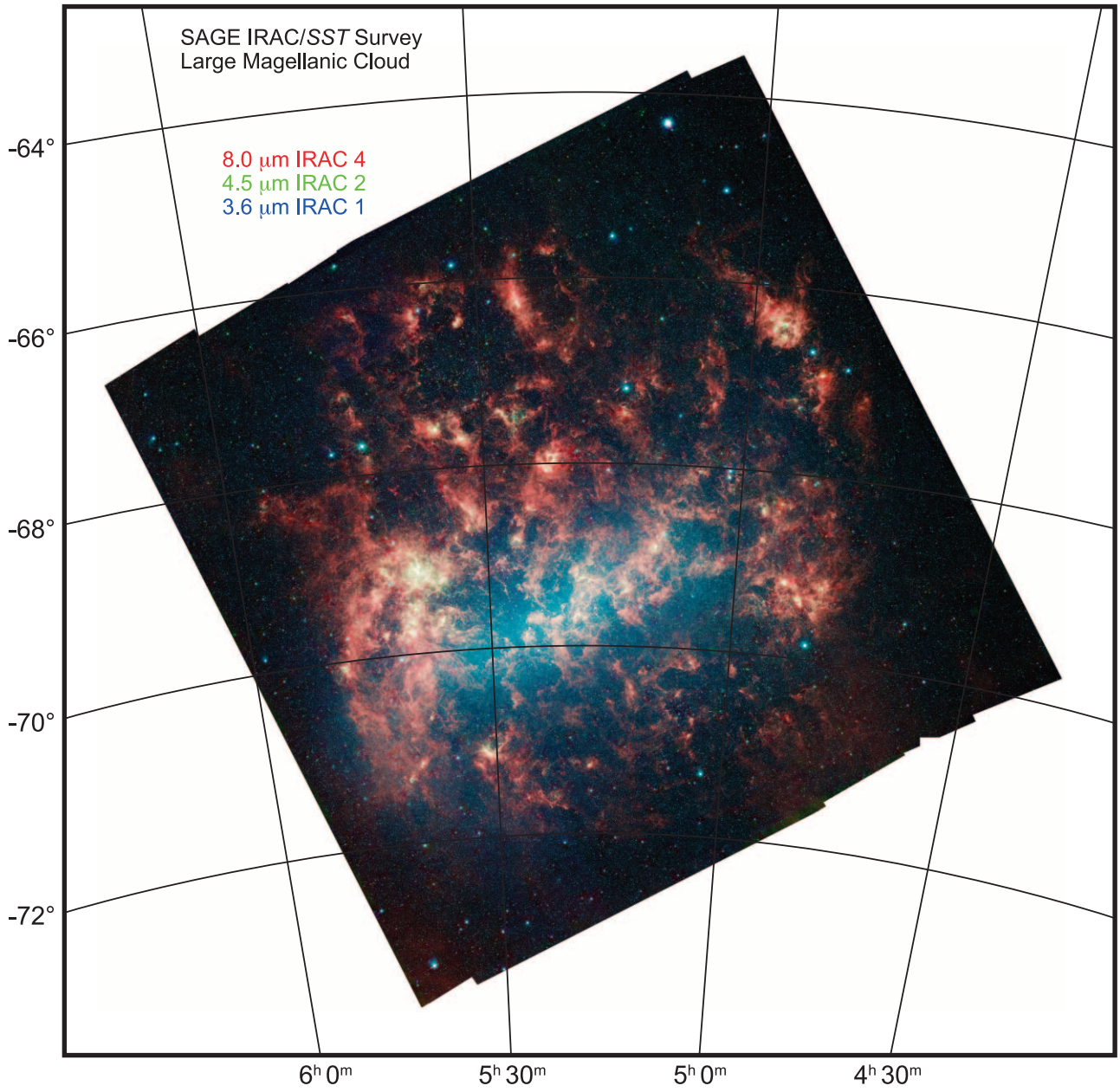

FIG. 3a

FIG. 3.—(*a*) Full LMC mosaics of the IRAC epoch 1 data of SAGE showing the location of the surveyed region on the sky. The IRAC data are shown in three colors, with IRAC-1 3.6 μm in blue, IRAC-2 4.5 μm in green, and IRAC-4 8 μm in red. (*b*) Full LMC mosaics of the MIPS epoch 1 and 2 data of SAGE showing the location of the surveyed region on the sky. The MIPS data are shown in three colors, with 160 μm in red, 70 μm in green, and 24 μm in blue.

to process the GLIMPSE data (Benjamin et al. 2003) and was modified for this project to handle the HDR mode. Some details can be found in the GLIMPSE pipeline documents,[28] and more will be forthcoming in an IRAC pipeline-processing document (M. Meade et al. 2006, in preparation).

3.1.1. *Initial Image Processing*

Initial image-processing steps for photometry include masking hot, dead, and missing data pixels (using SSC-supplied flags). Pixels associated with saturated stars are masked using an algorithm generated by the GLIMPSE team. Several image artifacts documented by Hora et al. (2004) and the IRAC Data Handbook[29] are corrected by the Wisconsin pipeline. We correct for column pulldown, which is a reduction in intensity of the columns in which bright sources are found, in the [3.6] and [4.6] bands using an algorithm written by L. Moustakas (Great Observatories Origins Deep Survey team) and modified by GLIMPSE to handle variable backgrounds. Also in bands [3.6] and [4.5], we use a modified version of the bright-source artifact corrector[30] to improve the correction of muxbleed, which is a series of bright pixels along the horizontal direction on both sides of a bright source. In the [5.8] and [8.0] bands, we correct for banding, which are streaks that appear in the rows and columns radiating away from bright sources, using an exponential function.

Two bright-source artifacts are not removed: muxstripe, which is a variation in the level of column segments due to a very bright

[28] See http://www.astro.wisc.edu/glimpse/docs.html.
[29] See http://ssc.spitzer.caltech.edu/irac/dh/.
[30] See http://spider.ipac.caltech.edu/staff/carey/irac_artifacts.

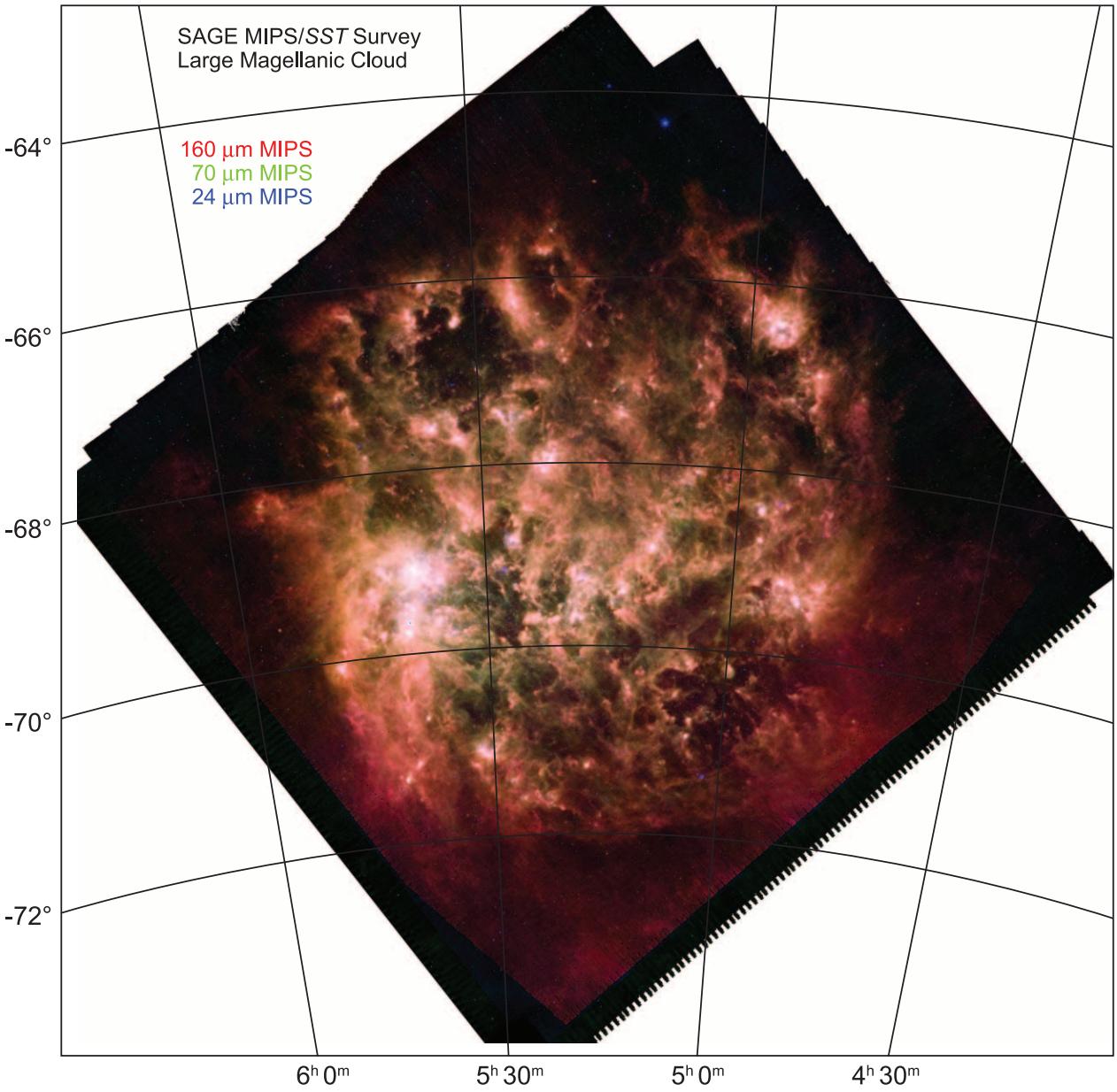

FIG. 3*b*

source, and latents, which are a persistence of a very bright source imaged in the prior IRAC frame.

Cosmic-ray rejection routines are not applied before photometry, since they often mask real stellar signal. These are applied prior to mosaic imaging, as discussed in § 3.1.6.

3.1.2. *IRAC Photometry*

The epoch 1 data shown in this paper consist of two visits on each sky position for each of the long and short exposures. Photometry was performed on individual frames and then combined in the SSC band-merger stage. In the future, when all the data are processed, photometry will be performed on the stacked mosaic images.

We use a modified version of DAOPHOT ALLSTAR (Stetson 1987) to perform PSF-fitted point-source photometry. We iterate on the photometric calculations to improve the flux estimates. Initially, sources are found at a 3 σ level above the local background. The local background is estimated by smoothing the image that contains sources, sky, and nebular emission. The found point sources are extracted by ALLSTAR. ALLSTAR does PSF fitting, simultaneously fitting all sources found on the image. It is an iterative process, minimizing the χ-value of the fit for each source. Sources that have converged and have a S/N greater than 2 are subtracted from the working image, producing a residual image. After every third iteration, the estimate of the local background for each remaining (unconverged) source is recalculated from the working image. After a maximum of 200 iterations, any remaining unconverged sources are deleted from the source list. Extracted sources then pass a second round of photometric processing. By doing small-aperture photometry on the residual image at the location of every extracted source, one can assess whether the extracted sources are over or undersubtracted. For benign flat-sky regions, aperture photometry of the residual image produces zero flux. However, in complex nebular regions in which background determination is more problematic, this

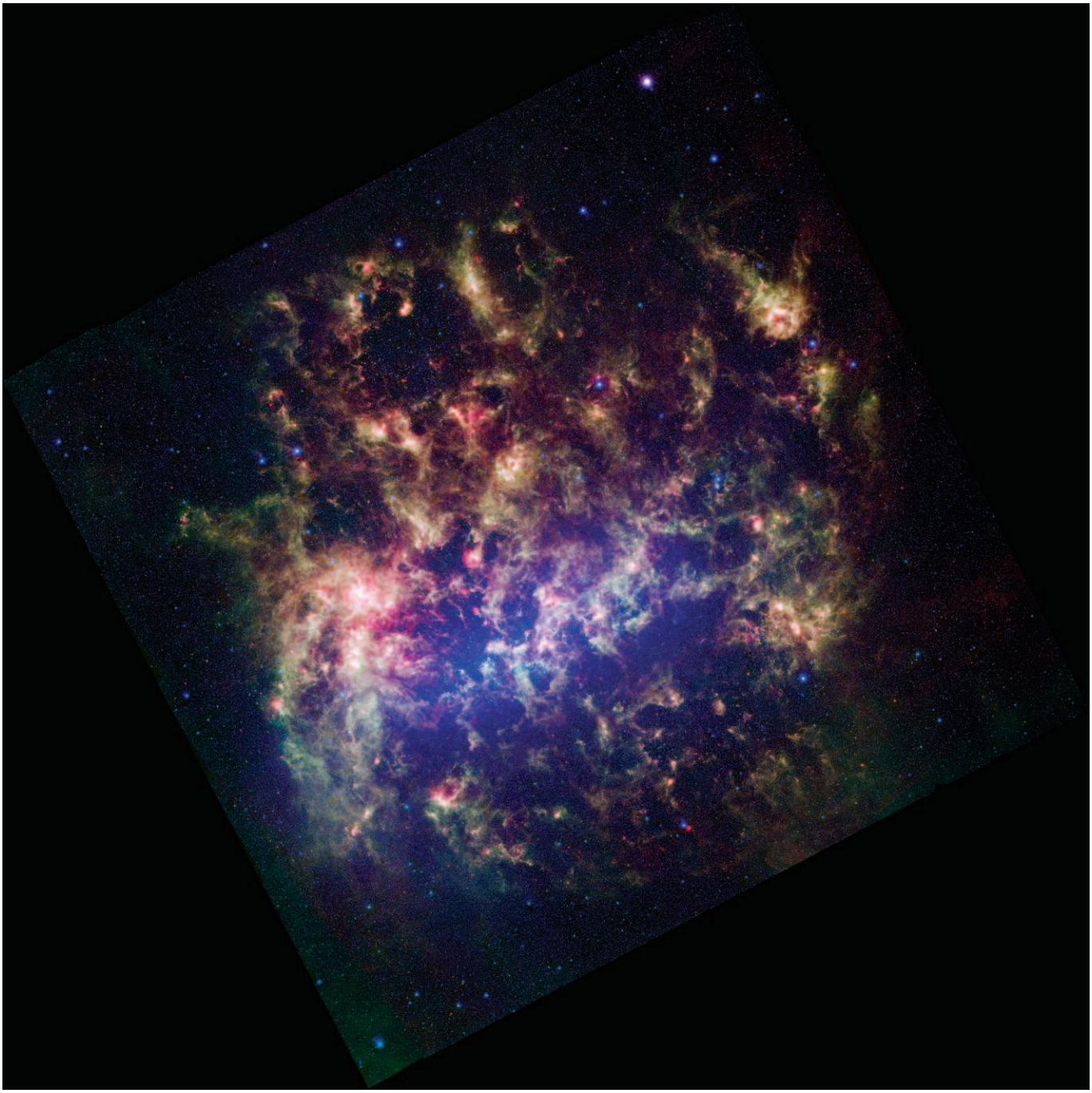

FIG. 4.—Full LMC mosaic of the SAGE data shown in three colors: epoch 1 IRAC-1 3.6 μm in blue, IRAC-4 8 μm in green, and MIPS 24 μm in red.

method has been effective in identifying sources that have been oversubtracted or undersubtracted by the ALLSTAR routine. The flux of those sources is then modified appropriately by the aperture photometry result.

Bright cosmic rays are removed from the point-source list based on an algorithm that operates on the residual images. A bright cosmic ray when extracted as a source will generally produce a characteristic signature in the residual image: a strong central peak surrounded by a negative (donut) background. Our software detects these signatures and removes the corresponding objects from the source list. Diagonal and faint cosmic rays are more problematic. Thus, our current source lists have strict S/N requirements to eliminate the faint cosmic rays from being accidentally included in our catalog, as described in § 3.1.4.

3.1.3. *Bandmerging to Produce Source Lists*

The point-source lists are merged at two stages using a modified version of the SSC band-merger stage.[31] Before the first stage, source detections with S/Ns less than 3 are culled. In addition, sources with 0.6 s exposure time fainter than magnitude 12, 11, 9, and 9 in the four IRAC bands [3.6], [4.5], [5.8], and [8.0], respectively, are culled to prevent Malmquist bias from affecting the results. During the first stage, "in-band merge," all detections at a single wavelength are combined using position, S/N, and flux to match the sources. The 0.6 s flux is included if the S/N is greater than 5, 5, 5, and 7 for the four IRAC bands [3.6], [4.5], [5.8], and

[31] See http://ssc.spitzer.caltech.edu/postbcd/bandmerge.html.

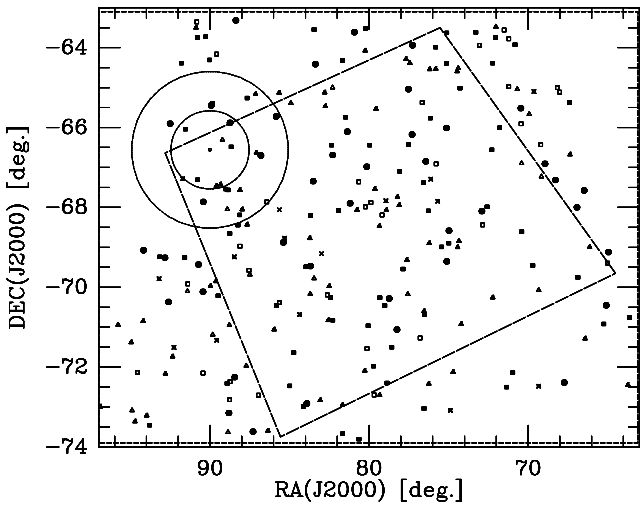

FIG. 5.—Locations of the SAGE absolute photometric standards calibration network listed in Table 3. The trapezoid box is the approximate location of the SAGE survey area adequate to cover SAGE's IRAC and MIPS observations. The two dotted circles represent stars within roughly 1° and 2° of the south ecliptic pole. Any such stars will be of gratuitous value to other missions observing the ecliptic poles, such as the *Wide-Field Infrared Survey Explorer* and the *James Webb Space Telescope*. Both of these are subsets of the short-dashed box, which encompasses the entire field of view, that indicates the area searched for appropriate calibration stars using SIMBAD. Symbols indicate the quality of each stellar calibrator, with the best being the filled circles, followed by filled squares and then filled triangles. These show consistency between optical and near-IR (2MASS) photometry and the spectral type and extinction to within 0.010, 0.030, and 0.060 mag, respectively. Open squares, open triangles, and open stars represent lower ranked calibrators with consistency at the levels of 0.090, 0.12, and 0.15 mag, respectively.

[8.0], respectively. The 12 s flux is included if the magnitude is fainter than the saturation limit of 9.5, 9.0, 6.5, and 6.5 for the four IRAC bands [3.6], [4.5], [5.8], and [8.0], respectively. When both criteria are met, the 0.6 and 12 s fluxes are combined, weighted by the propagated errors.

The second stage, "cross-band merge," combines all wavelengths for a given source position using only position as a criterion in order to avoid source color effects. In the cross-band merge stage, we also merge with the 2MASS catalog.[32]

3.1.4. *IRAC Catalog Criteria*

To ensure high reliability of the final point-source catalogs by minimizing the number of false sources, we adopt the following selection criteria: given M detections out of N possible observations, we require that $M/N >= 0.6$ in one band and $M/N >= 0.4$ in an adjacent band, with a S/N > 5, 5, 5, and 7 for IRAC bands [3.6], [4.5], [5.8], and [8.0], respectively. As an example, a source is typically observed twice at 0.6 s and twice at 12 s for a total of four possible observations in each band. Such a source detected three times in band [3.6] with S/N > 5 and twice in band [4.5] with S/N > 5 would be included in the catalog.

A source may be reliably detected in one band (usually [3.6] or [4.5]) but have questionable flux in another (usually [5.8] or [8.0]). To ensure high-quality fluxes for each source, a flux/magnitude entry for a band in the catalog will be nulled, i.e., removed, for any of the four following reasons: (1) The source is brighter than the saturation magnitude limits 6.0, 5.5, 3.0, and 3.0 for IRAC bands [3.6], [4.5], [5.8], and [8.0], respectively. (2) The source location is flagged as near a frame edge, in a saturated star wing, or coincident with a bad pixel. (3) The S/N is less than 6, 6, 6, and 10 for IRAC bands [3.6], [4.5], [5.8], and [8.0], respectively, in order to mitigate Malmquist bias. (4) For 12 s only data, M/N is less than 0.6, in order to mitigate faint cosmic-ray detections. For example, if N is 2 (12 s only data), then M has to be equal to 2 or the flux is nulled. If all fluxes for a source are nulled, the source is removed from the catalog.

Note that these catalog criteria refer only to the epoch 1 catalog presented in this paper and the first publicly released data set, which is based on single-frame photometry combined during the band-merge stage. Future catalogs, combining both epochs and based on mosaic photometry, will have different criteria. Characteristics of the epoch 1 catalog are summarized in Table 2.

3.1.5. *Absolute Photometric Calibration*

To assure that our photometric calibration is uniform across the large area observed by SAGE and between different AORs, epochs, and wavelengths, we extract the photometry for a network of absolute stellar calibrators custom-built for SAGE. These are A0–A5 V or K0–M2 III stars selected from SIMBAD, and their surface density within the SAGE area is approximately three stars per square degree (Fig. 5). The techniques used to produce the complete UV to mid-IR absolute spectra are described by Cohen et al. (2003). Any stars showing inconsistency between optical photometry, spectral type and reddening, and 2MASS photometry were culled to produce the final list of 139 viable calibrators for the epoch 1 data. The dynamic range for any IRAC band and for the MIPS 24 μm band was roughly 1000, and the faintest calibrators have magnitudes of 10.7 in IRAC and 7.7 at 24 μm. The zero points are 1594, 1024, 666.7, 277.5, 179.5, 116.5, and 63.13 Jy for the magnitudes in the 2MASS J, H, and K_s and IRAC [3.6], [4.5], [5.8], and [8.0] bands, respectively. This calibration network goes down to 0.150 mag in "mean absolute deviation" as defined in Cohen et al. (2003). The entire list of calibrator stars used for verification of the SAGE catalog is given in the online version of Table 3, with the 2MASS and IRAC magnitudes derived for these stars.

[32] 2MASS is a joint project of the University of Massachusetts and the Infrared Processing and Analysis Center, California Institute of Technology, funded by the National Aeronautics and Space Administration and the National Science Foundation.

TABLE 3
SAGE CALIBRATION STARS FOR THE IRAC PHOTOMETRY

STAR NAME	R.A. (deg)	DECL. (deg)	2MASS			ERROR			SAGE	ERR	SAGE	ERR	SAGE	ERR	SAGE	ERR
			J	*H*	*K*	*J*	*H*	*K*	[3.6]	[3.6]	[4.5]	[4.5]	[5.8]	[5.8]	[8.0]	[8.0]
HD 268625	72.58023	−67.98655	8.493	7.762	7.568	0.023	0.051	0.026	7.474	0.023	7.604	0.027	7.53	0.021	7.489	0.021
HD 268943	76.11154	−67.29521	10.7	10.698	10.677	0.023	0.025	0.023	10.732	0.023	10.73	0.023	10.728	0.023	10.732	0.022
HD 269157	77.56449	−70.17776	6.821	5.948	5.72	0.018	0.031	0.016	5.689	0.024	5.85	0.029	5.737	0.024	5.704	0.021

NOTES.—Table 3 is published in its entirety in the electronic edition of the *Astronomical Journal*. A portion is shown here for guidance regarding its form and content. Units of right ascension are hours, minutes, and seconds, and units of declination are degrees, arcminutes, and arcseconds.

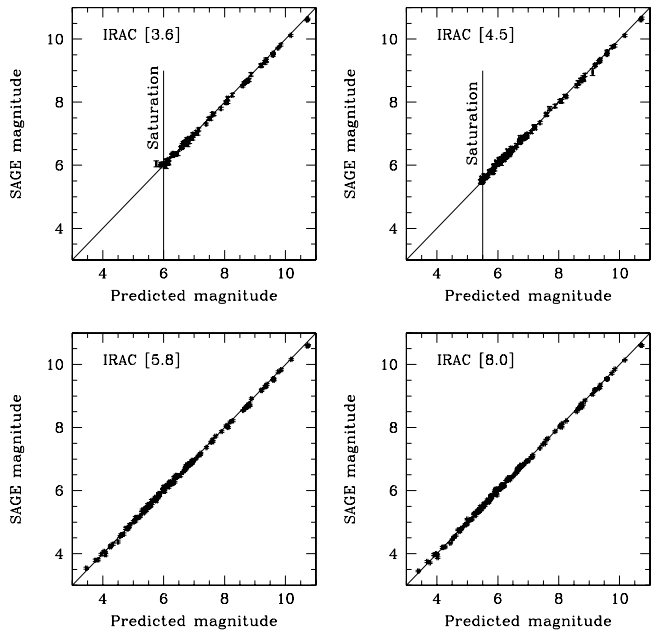

FIG. 6.—Plots demonstrating the quality of the SAGE flux and magnitude measurements in the epoch 1 IRAC point-source catalogs. For each IRAC band, noted in the top left of the plots, the measured SAGE magnitudes are plotted against the predicted magnitudes for the 139 calibration stars in the SAGE field. The size of the crosses represents the error bars on both axes.

Figure 6 shows the excellent agreement between the SAGE magnitudes and the predicted magnitudes of the calibration stars for the IRAC data. The magnitudes agree to within the 1 σ errors of our photometry, or approximately 5%.

3.1.6. *Mosaicked Images*

The individual IRAC epoch 1 images are further processed prior to mosaicking. Stray light areas were not masked in this data set, but will be masked when both epochs are included. Cosmic rays were removed using the dual-outlier rejection algorithms in the SSC MOPEX package. The 12 s images were mosaicked using the MONTAGE package.[33] The resulting full LMC IRAC images for epoch 1 are shown in Figures 3*a* and 4.

3.2. *MIPS Pipeline*

The MIPS Data Analysis Tool version 3.02 (DAT; Gordon et al. 2005) was used to do the processing and mosaicking of the individual images. The standard DAT reduction steps for MIPS 24 μm data are read2 correction, droop correction, dark subtraction, electronic nonlinearity correction, flat-fielding, flux calibration, distortion correction, cosmic-ray rejection, and mosaicking. The standard DAT reduction steps for the MIPS 70 and 160 μm data are read rejection (autoreject, missing, and saturated reads), electronic nonlinearity correction, ramp jump detection (cosmic rays), ramp line fitting, correction for response variations using the frequent stimulator measurements, dark subtraction, correction of the illumination pattern of the simulator, flux calibration, distortion correction, residual cosmic-ray detection, and mosaicking. Details of the standard DAT reduction steps can be found in Gordon et al. (2005).

In addition to the standard reductions and before mosaicking, extra processing steps on each image were carried out using programs written specifically to improve the reduction of large, well-resolved galaxies. In particular, at 24 μm, several extra steps were included. First, possible readout offset is corrected because one out of four readouts drifts slightly. Second, the array-averaged background flux value is subtracted from each MIPS AOR using data in the AOR. This "background" subtraction is intended to remove non-LMC diffuse emission, e.g., zodiacal or MW foreground diffuse emission, from the fast-scan leg. The background equals the average of the pixels in the MIPS AOR that are located off the LMC, defined as the most IR-bright edge (see, e.g., the IRAS image in Fig. 1). The subtraction makes the non-LMC emission equal to zero off of the LMC. Third, the processing excludes images affected by saturation sources, e.g., persistence that appears in a frame after a source has saturated the detector. Finally, the first five images in each scan leg are excluded because of transients associated with the boost frame. At 70 and 160 μm, a pixel-dependent background was subtracted from each fast-scan leg. This 70 and 160 μm "background" is composed of real emission from the zodiacal or MW foreground and instrumental drifts during the fast-scan leg. The background is derived using a low-order polynomial fit to the data in all the legs of each AOR that is outside of the LMC. At 160 μm, a spatial detection of cosmic rays is used to identify and remove them because there are too few frames to remove them by stacking the images.

The mosaicked images presented in Figures 3*b*, 4, 7, and 9 are a combination of the epoch 1 and 2 data. The additional redundancy improves cosmic-ray rejection and helps to minimize the striping artifacts.

3.2.1. *MIPS Point-Source Catalog*

The point sources in the mosaicked images of each AOR were extracted using the PSF-fitting program StarFinder (Diolaiti et al. 2000), which is suited for well-sampled PSF photometry in the variable-background regions that are found in MIPS data. The background in the case of these photometry measurements is the diffuse IR emission from the LMC surrounding the source. The removal of this background from the photometry measurements is handled with the same iterative approach as the IRAC photometry, albeit implemented with different programs. In these high-background photometry iterations, the sky plus nebular emission background is subtracted, and the photometry is done on the background-subtracted images. On the first iteration, the background is estimated by smoothing the image and subtracting the smoothed image from the original image. The point sources were extracted from this background-subtracted image. For the second and final iteration, the background is reestimated by smoothing a point-source-subtracted image, and the photometry is performed again on the new background-subtracted image.

For each MIPS band, a point-source list was created using a smoothed STinyTim, $T = 100$ K PSF with 3 σ and 0.80 correlation cuts in detected sources. The MIPS point-source catalogs are created by merging from each AOR, and the point-source lists are produced from multiple AORs. For sources detected in multiple AORs, the fluxes are averaged. The zero points for the magnitudes reported in Table 1 are 7.25, 0.82, and 0.16 Jy for MIPS bands 24, 70, and 160 μm, respectively. Three separate MIPS catalogs, one for each of the MIPS bands, 24, 70, and 160 μm, were produced but not merged because the angular resolutions of these MIPS catalogs differ substantially.

3.3. *SAGE Database*

We are using a relational database management system to query the SAGE IRAC and MIPS point-source catalogs. The database

[33] MONTAGE is funded by the National Aeronautics and Space Administration's Earth Science Technology Office. See http://montage.ipac.caltech.edu.

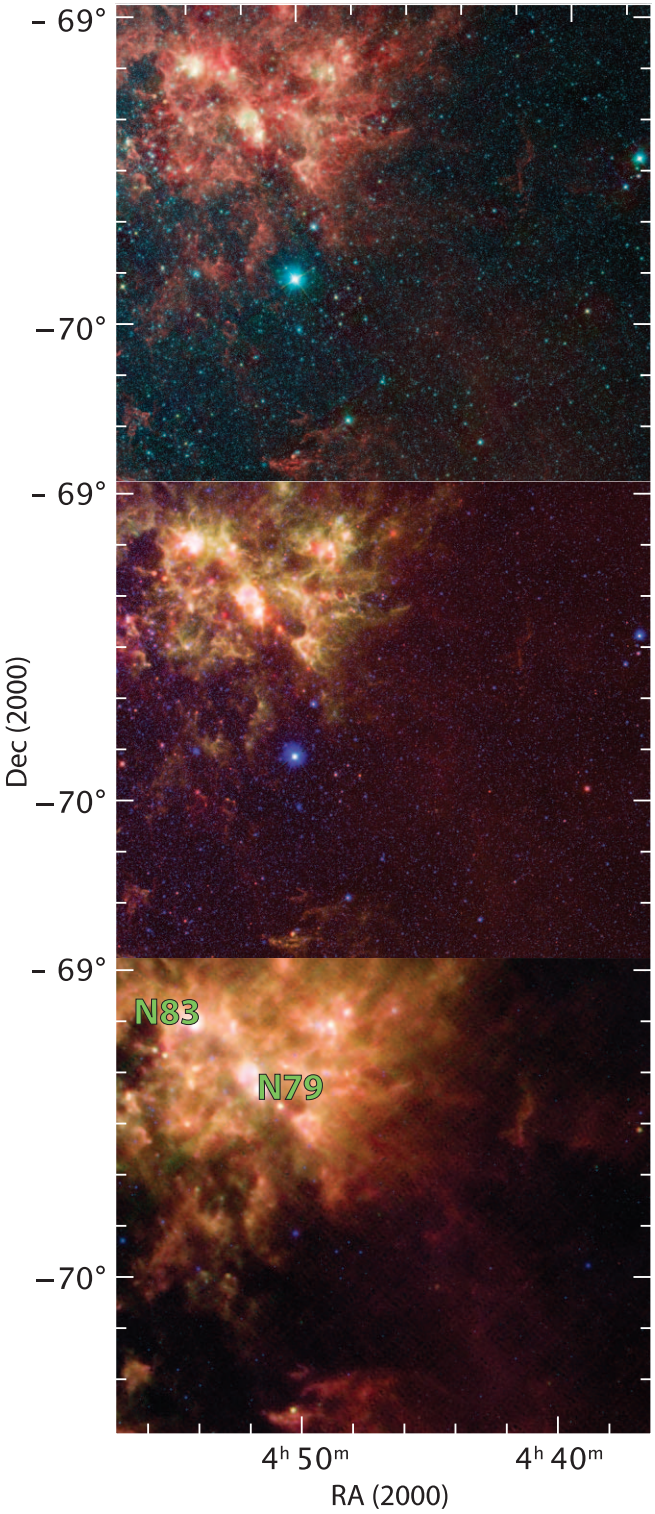

FIG. 7.—Three-color SAGE images of the N79/N83 region near the southwest end of the LMC bar. *Top*: IRAC three-color image, with IRAC-1 3.6 μm in blue, IRAC-3 4.5 μm in green, and IRAC-4 8 μm in red. *Middle*: IRAC 3.6 μm in blue, IRAC 8 μm in green, and MIPS 24 μm in red. *Bottom*: MIPS three-color image, with 160 μm in red, 70 μm in green, and 24 μm in blue. In all panels white is a combination of all three colors.

system is implemented with Microsoft SQL server 2000, which uses a structured query language as the basis for the queries.

The SAGE IRAC and MIPS point-source catalogs are ingested into the database system. The data can be queried using any of the catalog table parameters; for example, by position using cone searches, by flux or magnitude ranges by matching sources between catalogs, or any combination of these searches. The query interface includes a simple interactive Web form for small, simple queries and a more complex query system called Catalog Archive Server Jobs System, an expert query tool developed by the Sloan Digital Sky Survey Collaboration. We have used the SAGE database system to create a merged catalog of the available epoch 1 data in the IRAC and MIPS 24 μm catalogs using a search box of 3″ and adopting the closest IRAC source as the match for each MIPS 24 μm source. We have also used the SAGE database system to make the queries for the initial results presented in this paper.

4. PRELIMINARY EPOCH 1 RESULTS FROM A REGION NEAR N79 AND N83

We have done a preliminary analysis of the epoch 1 SAGE data for a $1\overset{\circ}{.}62 \times 1\overset{\circ}{.}62$ subregion centered at R.A. = $04^{h}47^{m}39\overset{s}{.}3$ and decl. = $-69°43'06\overset{''}{.}7$, which includes N79 and N83 (Fig. 7). This N79/N83 region is located just off the western edge of the LMC bar, as shown by the square box in Figure 1. The N79/N83 region includes both old and young stellar populations with a reasonable density and thus provides a scientifically useful gauge for results from SAGE epoch 1 data. Indeed, this field was chosen because it provided the first available processed SAGE data that covered a range of stellar types. The N79 and N83 nebulae are H II regions that have received only minor attention in the literature; e.g., inclusion in chemical abundance studies (e.g., Vermeij & van der Hulst 2002). N83B has two highly excited, compact blobs, N83B-1 and N83B-2 (Heydari-Malayeri et al. 2001), which are compact H II regions associated with dozens of newly formed massive stars and suggest ongoing star formation activity in this region. The stellar populations surrounding N79 and N83 have not been subject to detailed IR studies at *Spitzer* wavelengths.

4.1. *Images*

The color images of the N79/N83 region (Fig. 7) provide an overview for the differences in the IRAC and MIPS band emissions, whereas the black and white images reveal the distribution of the individual IRAC (Fig. 8) and MIPS (Fig. 9) bands. In the IRAC three-color image (3.6, 4.5, and 8 μm; Fig. 7, *top*), the blue (3.6 μm) and green (4.5 μm) reveal the stars, whereas the red (8 μm) shows mainly the diffuse dust emission. The three-color IRAC 3.6 and 8 μm and MIPS 24 μm image (Fig. 7, *middle*) shows how the stars and ISM dust emission relate. The density of stars, the blue point sources, drops off toward the edge of the LMC. The 8 μm dust emission appears filamentary because it traces the turbulent ISM of this star formation region. The warm continuum dust emission appears at 24 μm, which is more concentrated toward the centers of the H II regions, in contrast to the 8 μm PAH emission, which appears more diffuse and even surrounds the 24 μm emission. In the MIPS three-color image (24, 70, and 160 μm; Fig. 7, *bottom*), white point sources, which are detected in all three MIPS bands, appear in the N79 and N83 H II regions as the tips of warm dust columns pointing toward the exciting stars and are probably the bright rims of globules externally illuminated by the newly formed stars. Two white points, located in the west of the image, may be background galaxies. The red points, which have been detected in the very sensitive 160 μm band only, are most likely background galaxies. Blue points, which have been detected in the 24 μm band only, could be evolved stars or background galaxies.

The IRAC images of this N79/N83 region reveal the location of the stars and the dust emission from warm dust and PAHs

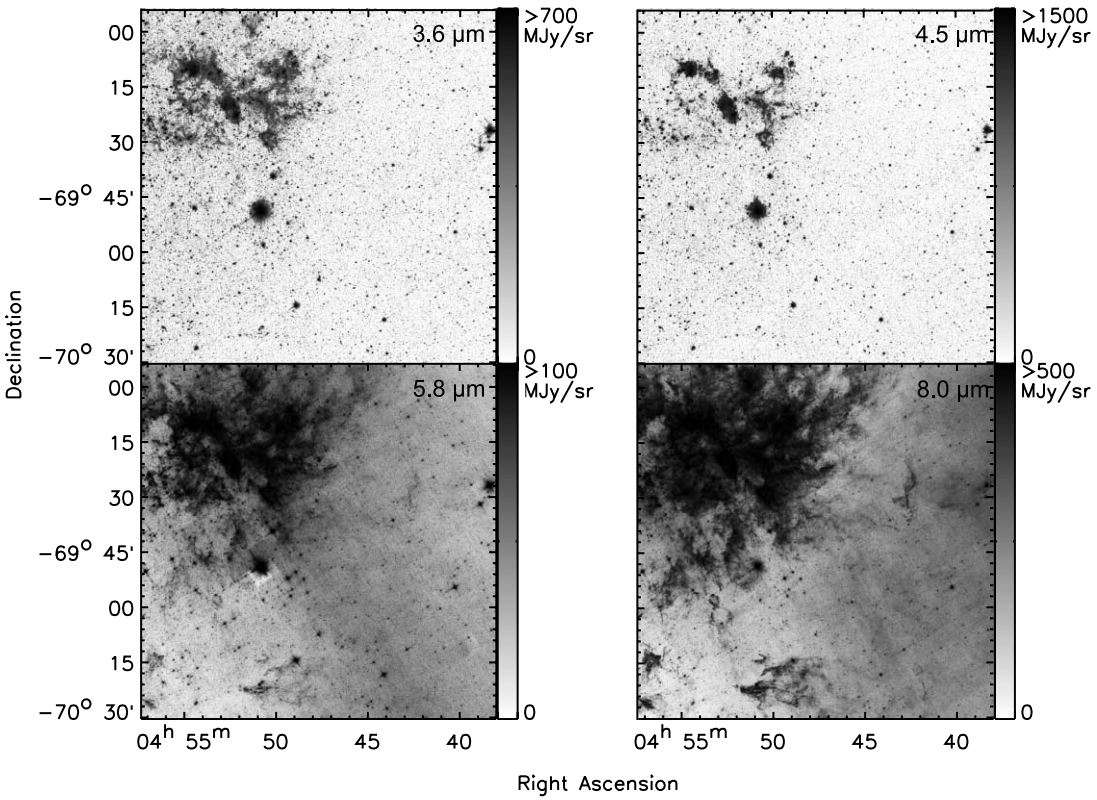

FIG. 8.—IRAC epoch 1 SAGE data of the region surrounding N79/N83. *Top left*: IRAC 3.6 μm. *Top right*: IRAC 4.5 μm. *Bottom left*: IRAC 5.8 μm. *Bottom right*: IRAC 8.0 μm.

(Fig. 8). The 3.6 and 4.5 μm images appear similar to each other with stars dominating the images and diffuse emission apparent only in the N79 and N83 nebulae, which are also the brightest regions in the longer *Spitzer* wavelengths. The origin of diffuse emission at 3.6 μm is likely to be bound-free continuum from the ionized gas with some contribution from the 3.3 μm PAH feature emission and very small dust grain emission (e.g., Engelbracht et al. 2006). The 4.5 μm diffuse emission is a combination of Brackett α, bound-free continuum, and possibly very small dust grain emission. As we progress to the longer IRAC wavelengths, the diffuse emission becomes more prominent and the number of stars decreases. The 5.8 μm band emission is only slightly brighter than the 3.6 and 4.5 μm emission. The origin of the 5.8 μm diffuse emission is most likely very warm dust emission ($T \sim 600$ K) with contributions from the 5.6 and 6.2 μm PAH feature emissions. The 8 μm band diffuse emission is substantially brighter and more extended than the shorter IRAC bands. Also, diffuse 8 μm band emission can be seen in regions well off the N79 and N83 H II complexes. The origin of the 8 μm diffuse emission is most likely the 7.7 and 8.6 μm PAH features.

The MIPS 24, 70, and 160 μm images show primarily dust emission of the region (Fig. 9). The diagonal striping artifact at 70 and 160 μm has been minimized but not eliminated in these combined epoch 1 and 2 data. Point sources are detected in all the bands but with a substantially decreasing number compared to IRAC images. At first glance, the MIPS images have similar structures, with the main difference being the smoother appearance at longer wavelengths due to the lower angular resolution. Closer inspection shows that the more diffuse, cirrus dust emission that is located farther from the star formation is relatively brighter at 160 μm compared to 24 μm. In the oversimplified case of blackbody dust grain emission, grains at approximately 120, 40, and 20 K have peak blackbody emission at 24, 70, and 160 μm, respectively, with the 120 K grains being the most emissive at all wavelengths. Thus, in such an oversimplified case, we expect the dust to be hottest near the massive star formation regions and emit brightly at 24 μm compared to the dust in the diffuse ISM, which is significantly cooler but that would still emit brightly at 160 μm. Of course, dust grains have a size distribution with the very smallest grains or PAHs being susceptible to nonradiative equilibrium emission. A model comprising PAHs, very small grains, and large grains has been successful at explaining the cirrus emission at 12 and 25 μm in the MW (e.g., Desert et al. 1990) and could potentially explain the presence of 8 and 24 μm *Spitzer* emission in the diffuse dust emission observed in the southwestern part of this region.

4.1.1. *Comparison with ISM Gas Tracers*

One of the scientific goals for SAGE is to understand the mixing of dust into the ISM and how the dust properties vary across the LMC. For such studies it is useful to compare the dust emission to tracers of gas, and here we take a preliminary look at this comparison for the N79/N83 region. Quantitative analysis of these data is beyond the scope of this paper; however, the visual comparison provides some qualitative insight. Figure 9 shows a comparison of the MIPS 24, 70, and 160 μm dust emission with three tracers of interstellar gas: Hα line emission from the Southern Hα Sky Survey Atlas (SHASSA; Gaustad et al. 2001), H I 21 cm line emission (Staveley-Smith et al. 2003; Kim et al. 2003), and CO $J = 1-0$ line emission (Fukui et al. 2001; Y. Fukui et al. 2006, in preparation). At first glance, the dust emission revealed by MIPS bears more resemblance to the H I 21 cm line emission image than the Hα or CO. The diffuse extended emission found in the H I 21 cm line images is also seen in the MIPS 70 and

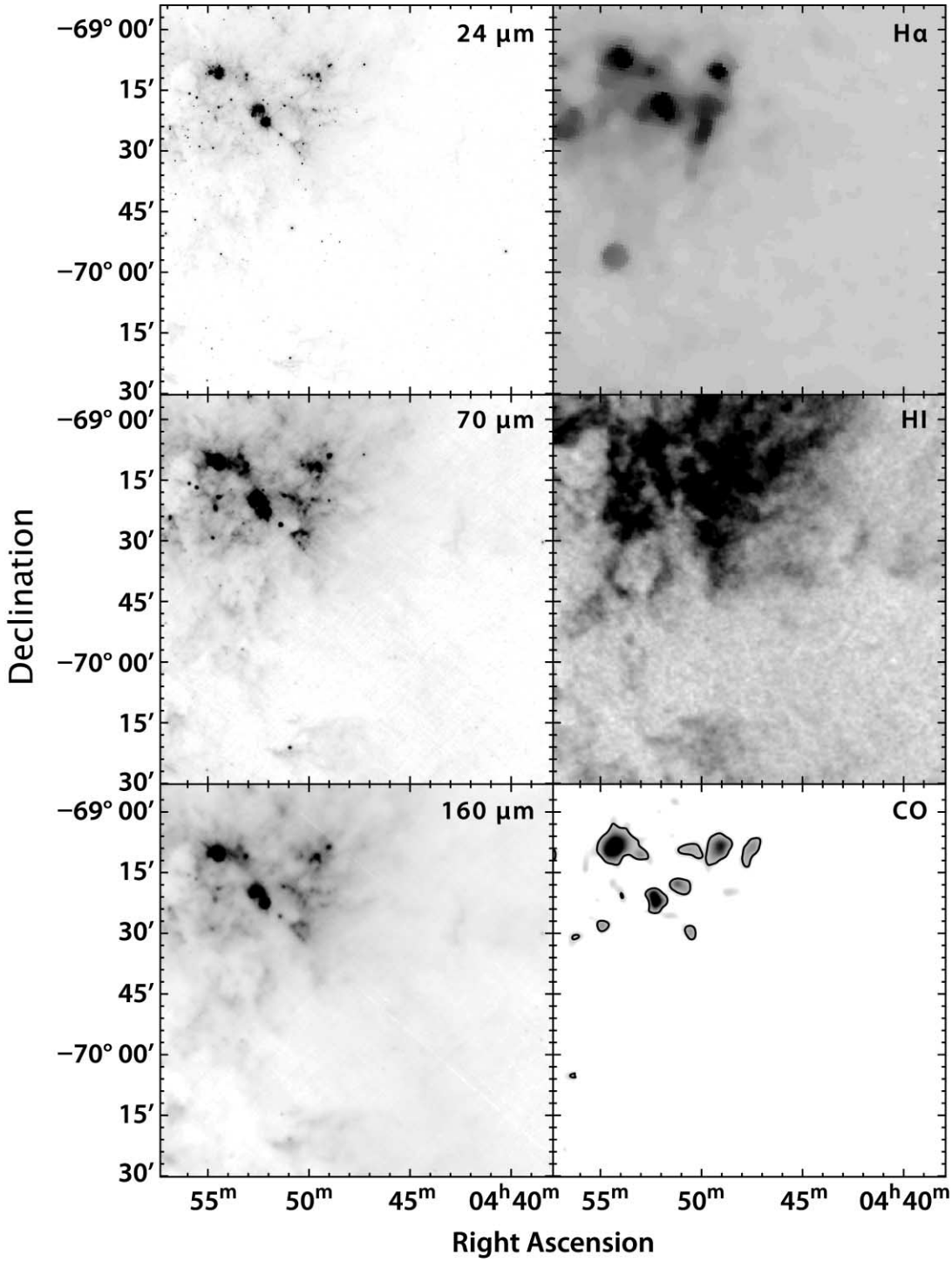

FIG. 9.—MIPS epoch 1 SAGE data of the N79/N83 region in comparison with ISM gas tracers. *Top left*: MIPS 24 μm with a square-root gray scale ranging from 0 to 20 MJy sr^{-1}. *Middle left*: MIPS 70 μm with a square-root gray scale ranging from 0 to 100 MJy sr^{-1}. *Bottom left*: MIPS 160 μm with a square-root gray scale ranging from 0 to 300 MJy sr^{-1}. *Top right*: Hα SHASSA data in a log scale (Gaustad et al. 2001). *Middle right*: H I 21 cm line data in a square-root gray scale (Staveley-Smith et al. 2003; Kim et al. 2003). *Bottom right*: CO $J = 1-0$ line data in a square-root scale where the contour marks the 3 σ level (0.7 K km s^{-1}) and the data are absent from the lower right (southwest) part of the image (Fukui et al. 2001; Y. Fukui et al. 2006, in preparation).

160 μm bands and suggests that the large dust grain emission is probably well mixed with the gas. In contrast to the H I, the Hα and CO emissions are highly structured and mostly confined to the massive star formation regions. In these H II regions, the dust emission detected by MIPS, especially the 24 μm band, exhibits very bright peaks that are not seen in the H I 21 cm line emission but that coincide with the concentrations of Hα and CO emission. These bright 24 μm peaks reveal regions of very warm ($\sim$120 K) dust heated by the young, massive stars, and the gas peaks indicated by the CO and Hα reveal that these hot-dust regions coincide with high gas densities. Interestingly, the IRAC 8.0 μm emission, which traces PAHs, appears well correlated with the H I 21 cm gas emission but absent from the star formation regions, suggesting that the PAHs are modified or destroyed in

these regions (Fig. 8). Thus, the dust emission revealed by the combined MIPS 24, 70, and 160 μm bands and the IRAC 8.0 μm band traces all three phases of the ISM gas; however, the relative intensity of these dust emission bands varies with the ISM environment.

4.2. *Point-Source Limits and Source Counts*

The point-source lists are derived from the IRAC and MIPS data for a circular region centered at R.A. = $04^{h}47^{m}39\overset{s}{.}3$ and decl. = $-69^{\circ}43'06\overset{''}{.}7$ with a $0\overset{\circ}{.}81$ radius, which would define a circle inscribed in the IRAC and MIPS images of the N79/N83 region (Fig. 7). These point-source lists have been analyzed to determine the broad characteristics of the detection rates in this region and anticipated characteristics of the entire SAGE survey for epoch 1. Table 2 lists the characteristics for the SAGE survey based on the epoch 1 point-source extractions for the N79/N83 region. Column (1) of Table 2 lists the SAGE band for which the following columns apply. If there is more than one SAGE band in this column, then the results are a Boolean "AND" for all the bands. Columns (2) and (3) of Table 2 list the detected fluxes and magnitudes of the faintest sources found in the epoch 1 catalogs and provide an estimate for the final epoch 1 catalog for SAGE. These epoch 1 limits are expected to be less sensitive than the final catalogs because they have less integration time than the complete survey and because systematic errors due to image artifacts are not completely removed.

The point-source counts from the epoch 1 catalog for this field are listed in column (4) of Table 2. These counts are highest at 3.6 μm, with 119,333 detected, and decrease dramatically toward longer wavelength, with only 46 detections at 160 μm. This trend is consistent with expectations. The most numerous point sources, stars, show up best at 3.6 μm, whereas at longer wavelengths their contributions diminish rapidly because the photospheric emission on the Rayleigh-Jeans tail declines rapidly at longer wavelengths. The longer *Spitzer* wavelengths have increased source crowding due to the larger beam and reduced contrast between the point sources and the relatively brighter background of the local ISM. The point sources that appear at the longer *Spitzer* wavelengths have a significant amount of dust emission associated with them, such as YSOs, evolved stars, and background galaxies. At the bottom part of Table 2, the source counts for combinations of *Spitzer* bands are presented. The largest number appears for sources with both IRAC 3.6 and 4.5 μm detections, as expected because these bands most effectively trace the stellar population of the region. Sources with detections in all four IRAC bands are down by a factor of $\sim$20 from just 3.6 and 4.5 μm. When one requires detection in all IRAC bands and MIPS 24 μm, the source counts decrease by a factor of $\sim$90 from all IRAC bands alone. The 1175 sources detected at 3.6, 8.0, and 24 μm are used for the source classification described in § 4.3. Clearly, the type and quantity of sources that we are detecting varies tremendously based on the color selection criteria. In particular, the cooler and more dusty sources, i.e., ones with MIPS counterparts, are rare in comparison to the stellar population.

Lower limits for the total number of epoch 1 sources in the SAGE survey are listed in column (5) of Table 2. To derive these lower limits, we simply scaled the source counts from this N79/N83 region by $(7\overset{\circ}{.}1 \times 7\overset{\circ}{.}1)/\pi(0.81)^2 = 24.5$; i.e., the ratio of the angular areas of the whole survey to that of the N79/N83 region. The total number of sources anticipated in the SAGE survey is >2.92 million in the 3.6 μm band for the epoch 1 point-source catalogs. For IRAC, we can compare these counts to the total number of sources in the epoch 1 catalog that are listed in column (6) of Table 2. We find that the actual total number of sources in the epoch 1 catalog is larger by a factor of $\sim$1.38 compared to the estimate. This discrepancy is not surprising because the N79/N83 region of the SAGE survey has a lower density of sources compared to the rest of the LMC (e.g., Westerlund 1997, p. 234). For the combined epoch 1 and 2 final catalog, we expect much higher detection rates because the source extraction will go deeper.

For IRAC, the epoch 1 sensitivities listed in Table 2 are largely limited by our catalog source selection criteria that rejects faint cosmic rays as well as real faint sources (see § 3.1.4). Thus, our current limiting sensitivities are higher than those predicted based on an exposure time calculator (SENS-PET), which assumed an isolated point source in a medium background, not a realistic case for all locations in the LMC. This limitation will be removed in future source lists because the epoch 1 and 2 data will be combined with cosmic-ray rejection prior to photometry. Moreover, by stacking the images for the IRAC SAGE data we increase the final integration time by a factor of 4 and thereby improve the S/N by at least a factor of 2 or more if one considers the removal of the artifacts. Thus, we anticipate that our final point-source catalog will reach the predicted sensitivities and source counts.

For MIPS, the epoch 1 point-source catalog of which is still in progress for completion, the sensitivities reached for the 24, 70, and 160 μm bands (Table 2) are comparable to those predicted (Table 1). The final catalog, which will combine epochs 1 and 2, is expected to meet the predicted sensitivities because the integration time for epoch 1 is only half of the final, and thus a factor of $\sim$1.4 (= $\sqrt{2}$) improved sensitivity is anticipated.

4.3. *Source Classification Approach*

Detailed classification of all the detected sources is beyond the scope of this paper. In this section, we begin classification of the sources by applying some rough boundaries on the types of sources using templates defined for the MW. The Cohen (1993) MW templates, which were developed for *IRAS* data, have been adapted for the IRAC and 2MASS color classification scheme for GLIMPSE. Whitney et al. (2004) have developed YSO models for GLIMPSE. This MW classification scheme has been applied to the *MSX* sources of the LMC (Egan et al. 2001). These previous works include a wide range of IR source types such as main-sequence stars, red giants, O-rich AGB stars, C-rich AGB stars, OH/IR stars, dusty carbon stars, H II regions, planetary nebulae, and YSOs with a range of luminosities within each of these categories.

In this preliminary work, we employ the MW templates, which were adapted for the GLIMPSE project, to classify the SAGE sources on a [3.6] − [8.0] versus [8.0] − [24] color-color diagram (Fig. 10). While they may not be completely appropriate for the LMC, these MW templates are at least a well-understood starting point. On the [3.6] − [8.0] versus [8.0] − [24] color-color diagram we plot these MW templates in a simplified manner by grouping them into three broad categories: stars without dust (Fig. 10, *asterisks*), dusty evolved stars (Fig. 10, *triangles*), and YSOs (Fig. 10, *squares*). Stars without dust include main-sequence stars and red giants. Dusty evolved stars include the O-rich and C-rich AGB stars, OH/IR stars, and carbon stars. YSOs cover the range in mass and temperature and include H II regions and lower mass Class I–III sources.

The [3.6] − [8.0] versus [8.0] − [24] color-color diagram provides the widest range in color for SAGE point sources that still includes enough sources for a valid classification. The 1175 point sources detected at 3.6, 8.0, and 24 μm in the N79/N83 region are plotted on this color-color diagram and classified into one of the three categories as follows; using the MW templates as a guideline,

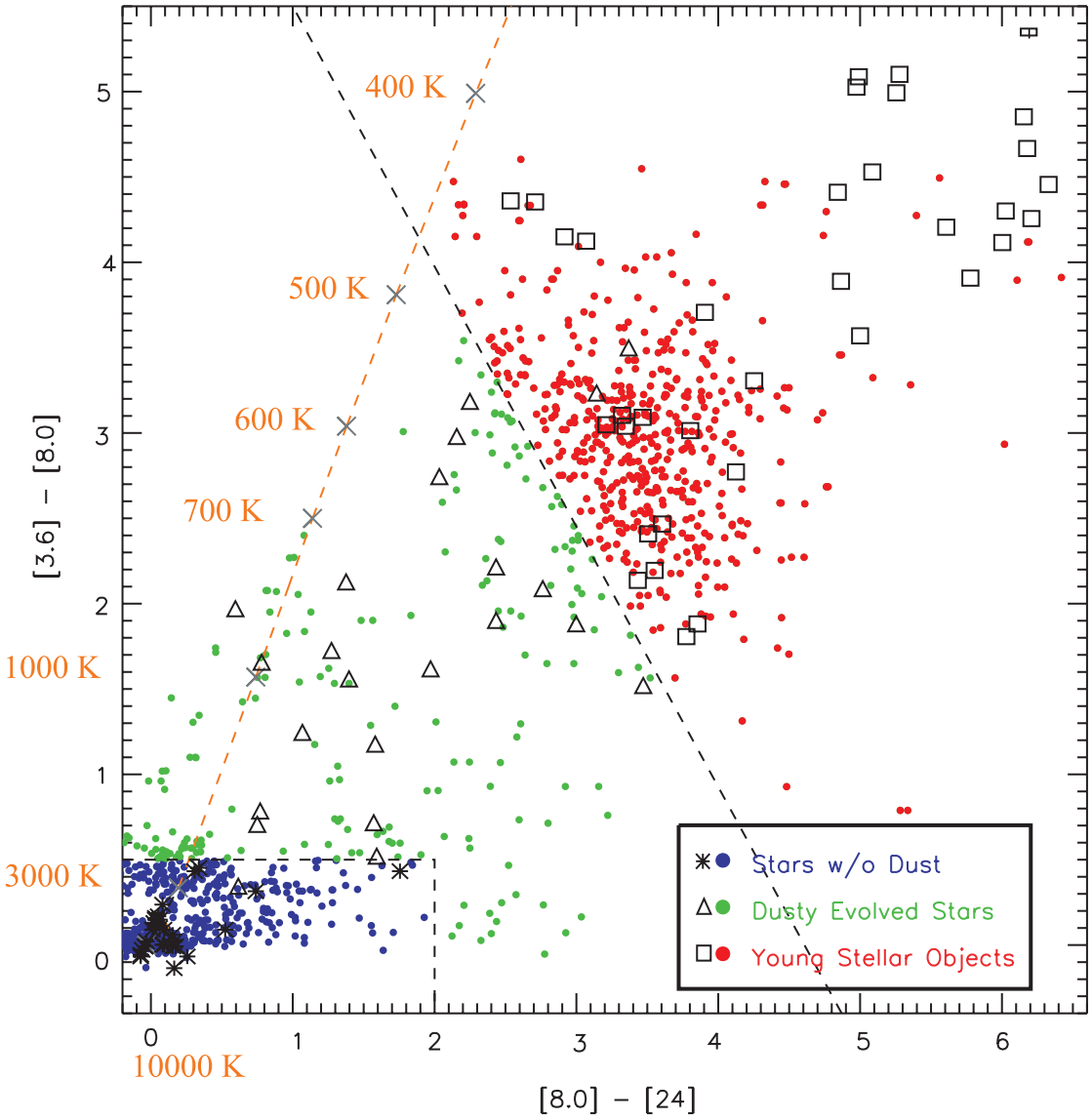

FIG. 10.—The [3.6] − [8.0] vs. [8.0] − [24] color-color diagram, showing the broadest separation of sources while still retaining enough sources to derive a source classification. For all bands, square brackets mean the Vega magnitude at that wavelength, e.g., [8.0] is the Vega magnitude at 8.0 μm. Black symbols represent MW templates from Cohen et al. (1993) and Whitney et al. (2004). Asterisks represent stars without dust, such as main-sequence stars or red giants. Triangles represent dusty evolved stars. Squares represent YSOs. The black dashed line marks the boundary for the source classification based on the location of the MW templates. The orange dashed line shows the color temperature for blackbodies with temperatures ranging from 10,000 to 400 K, marked as gray crosses on the line. The 1175 colored circles are point sources detected in IRAC 3.6 and 8.0 μm and MIPS 24 μm bands from the N79/N83 region. The red, green, and blue circles are candidate YSOs, dusty evolved stars, and stars without dust, respectively. These color-classified sources are plotted in the color-color diagrams and CMDs of Figs. 11 and 12, respectively, to provide guidance on the types of sources plotted.

we define some boundaries of regions of color space for the three categories:

1. Stars without dust are bounded by the lower left box $[8.0] - [24] < 2$ and $[3.6] - [8.0] < 0.5$ and shown in blue.
2. Dusty evolved stars are enclosed in $[3.6] - [8.0] < -1.525([8.0] - [24]) + 7.025$ and $[3.6] - [8.0] > 0.5$ and shown in green.
3. YSOs are defined by $[3.6] - [8.0] > -1.525(8-24) + 7.025$ and shown in red.

These boundaries are drawn as dashed lines on Figure 10. The points that lie in these different regions are considered candidates for this LMC subgroup, and below, when we state one of these subgroups by name, e.g., dusty evolved stars, we always mean candidates for this subgroup, e.g., candidate dusty evolved stars. A temperature line on this color-color plot shows that the temperature of the sources decreases from ~10,000 to 400 K as we progress from the lower left to upper right of the diagram. Alternatively, the IR dust emission from these sources increases in this progression. The YSOs are cooler than dusty evolved stars, which appear cooler than stars without dust. The stars without dust appear to have two populations that change in color temperature, one near ~10,000 K, which are most likely main-sequence stars, and one near ~3000 K, which are most likely red giant stars.

We plot two additional color-color diagrams for the N79/N83 region to see how our source classification holds up (Fig. 11). All the points are first plotted in black, and then those sources that were included in the source classification color-color diagram (Fig. 10) are overplotted with their corresponding color classification. The IRAC [3.6] − [4.5] versus [5.8] − [8.0] color-color diagram (Fig. 11, *left*) shows a similar separation of the source types

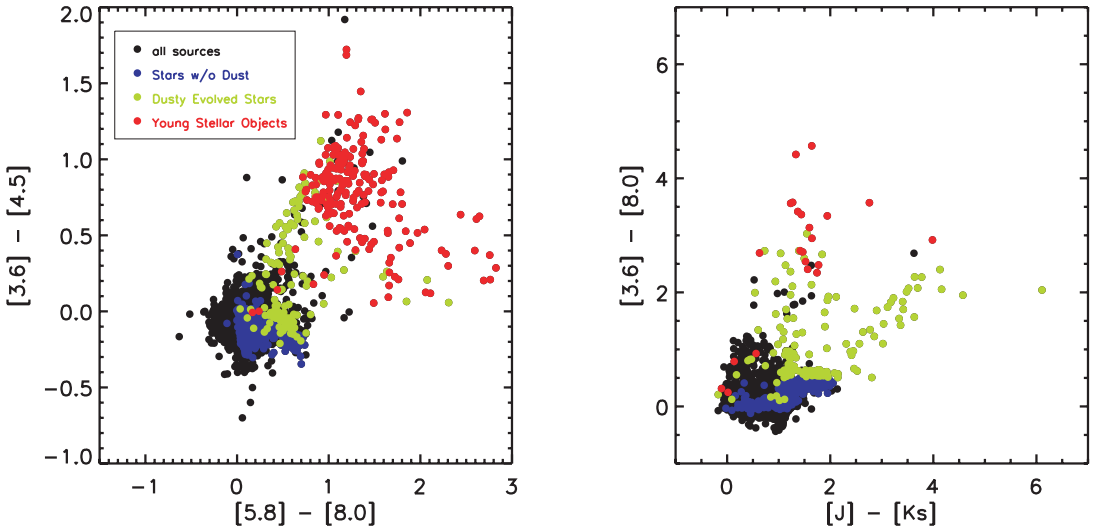

FIG. 11.—Color-color plots. *Left*: IRAC-only plot. *Right*: IRAC and 2MASS plot, showing how the source classification holds at other wavelengths for point sources detected in the SAGE N79/N83 region. The black circles are plotted first and include all the sources detected in the bands plotted. The colored circles are overlaid on the black circles and include the same circles as plotted in the source classification template (Fig. 10).

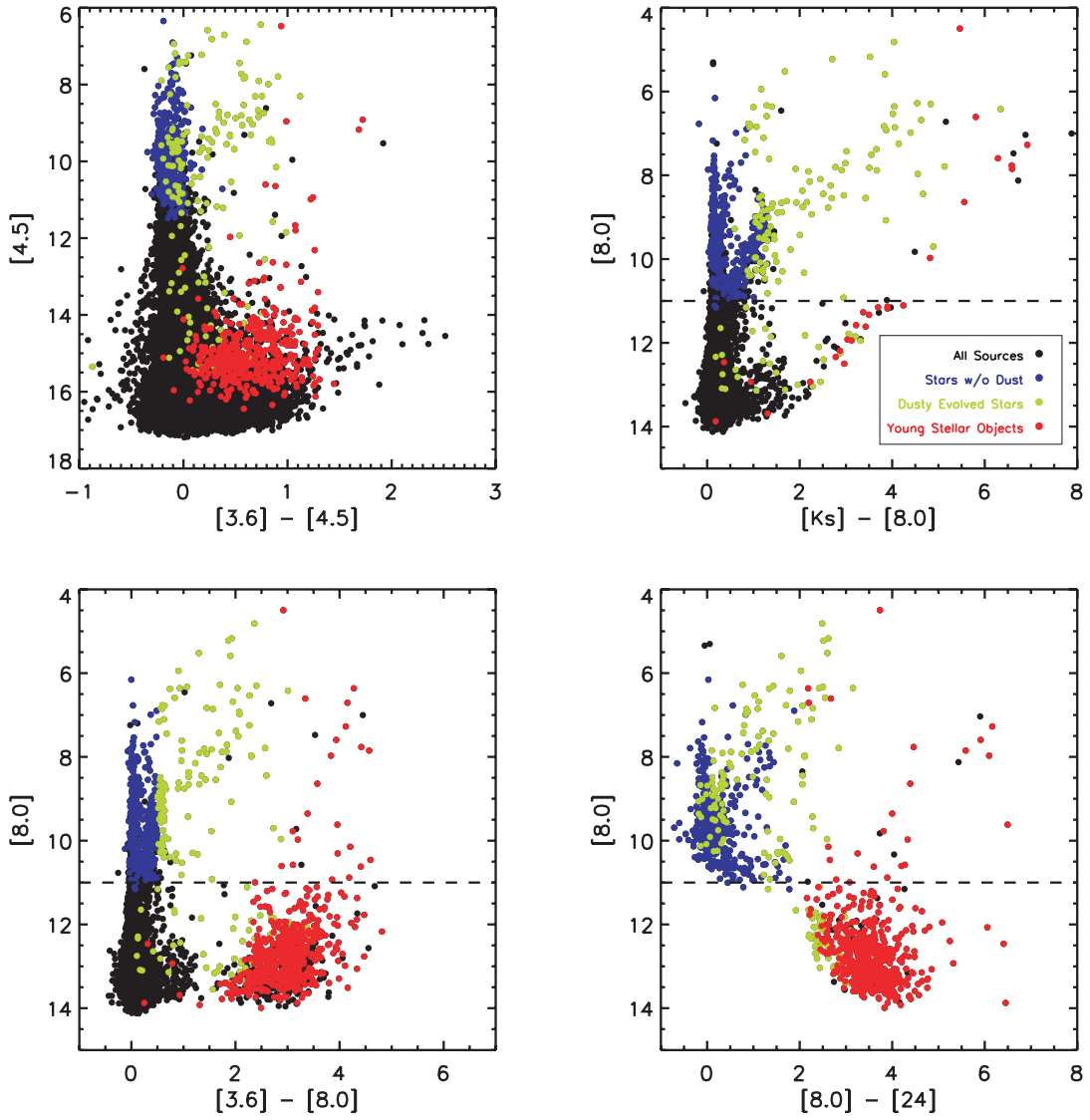

FIG. 12.—Four CMDs of SAGE data showing in black all the point sources from the N79/N83 region that have been detected at the wavelengths plotted in the CMD. The candidate classified sources from the source classification are overlaid in the same color used in Fig. 10. The black circles are sources detected in the bands of the CMD but not in all of the bands of the source classification diagram and hence tend to be fainter sources not detected at the longer wavelengths, e.g., 24 μm. The dashed line at [8.0] = 11 mag marks the mass-loss rate of $10^{-8}\ M_{\odot}\ \mathrm{yr}^{-1}$, above which the AGB stars appear to have dusty winds.

with some mixing of sources near the boundary, which only emphasizes that the boundaries we defined are not rigid but guiding. We also see a similar trend of the YSOs residing at the cooler colors. The number of stars without dust has increased in this IRAC-only plot. At even shorter wavelengths, the [3.6] − [8.0] versus $J - K_s$ color-color plot (Fig. 11, *right*) still shows relatively clear separation. The stars without dust appear in two populations, which were hinted at in the [3.6] − [8.0] versus [8.0] − [24] color-color diagram. In comparison to the IRAC-only color-color diagram, the numbers of dusty evolved stars and pre-main-sequence stars are significantly less, and the number of stars without dust are significantly more. This decrease is part of an overall trend in the source populations. The stars without dust are found primarily at the shorter wavelengths, and as we increase the wavelength coverage the population of dusty objects, i.e., dusty evolved stars and pre-main-sequence stars, increases in number.

4.3.1. *Color-Magnitude Diagrams*

One of the advantages of the LMC is that all stellar populations are at essentially the same distance, and thus, we can use CMDs as an additional way to separate and identify the sources. Figure 12 shows four CMDs for the N79/N83 region. The top left panel shows an IRAC [4.5] versus [3.6] − [4.5] CMD and reveals the multitude of sources detected by IRAC in this region. The top right panel shows an IRAC/2MASS CMD of [8.0] versus $[K_s]$ − [8.0] and shows how the addition of near-IR photometry can help separate the effects of dust from the stellar photosphere. The bottom two CMDs, [8.0] versus [3.6] − [8.0] (*left*) and [8.0] versus [8.0] − [24] (*right*), are repeats of Figure 2 but without all the MW templates. The dashed lines in the last three CMDs mark the limit of [8.0] = 11 mag, below which we expect LMC AGB stars to have little or no dusty mass loss (van Loon et al. 1999; see their Fig. 9; $M_{\rm bol} < -4.5$, assuming a bolometric correction to the [8.0] of 3 mag and a distance modulus of 18.5). The diagonal edges to the points plotted on these CMDs are caused by the sensitivity and brightness limits of the epoch 1 point-source catalog for SAGE. In particular, the faint limit of the 3.6 μm IRAC band affects the [4.5] versus [3.6] − [4.5] and [8.0] versus [3.6] − [8.0] CMDs; the faint limit of the K_s of 2MASS affects the [8.0] versus $[K_s]$ − [8.0] CMD, and the faint limit of the 24 μm MIPS band affects the [8.0] versus [8.0] − [24] CMD. The maximum brightness limit at 3.6 μm also affects the [8.0] versus [3.6] − [8.0] CMD.

The number of sources included in these CMDs is largest for the shortest wavelengths and decreases at the longer wavelengths (Fig. 12). As with the color-color diagrams, all the sources are first plotted in black and then those sources that were included in the source classification color-color diagram (Fig. 10) are overplotted with their corresponding color classification. Common to all CMDs is a locus of point sources with color zero, which includes mostly stars without dust, i.e., blue points. The brightest of these stars are most likely foreground MW stars (see § 4.4.2). Since the most limiting factor for inclusion in Figure 10 is detectability in the 24 μm MIPS band, the [8.0] versus [8.0] − [24] CMD contains, almost entirely, sources from Figure 10. At shorter wavelengths the number of black points increases with decreasing wavelength and fills in the fainter end of the locus of points at zero color. This trend is consistent with the fact that the shorter wavelengths of IRAC and 2MASS are sensitive to stellar photospheres of nondusty stars, whereas the additional constraint of a 24 μm MIPS band detection makes it a source of interest for the scientific goals of SAGE.

Common to all the CMDs, the stars without dust and the dusty evolved stars appear to dominate the bluer and brighter magnitudes, respectively, while the YSOs tend to occupy the redder and fainter magnitudes in all four CMDs. The fact that we detect few of these faint YSO candidates when we include the K_s of 2MASS demonstrates that the SAGE survey goes fainter than 2MASS. The YSO population is well separated from the stars without dust and dusty evolved star populations in the [8.0] versus [3.6] − [8.0] and [8.0] versus [8.0] − [24] CMDs. Although some are very bright and red, the bulk of the YSOs are faint and red.

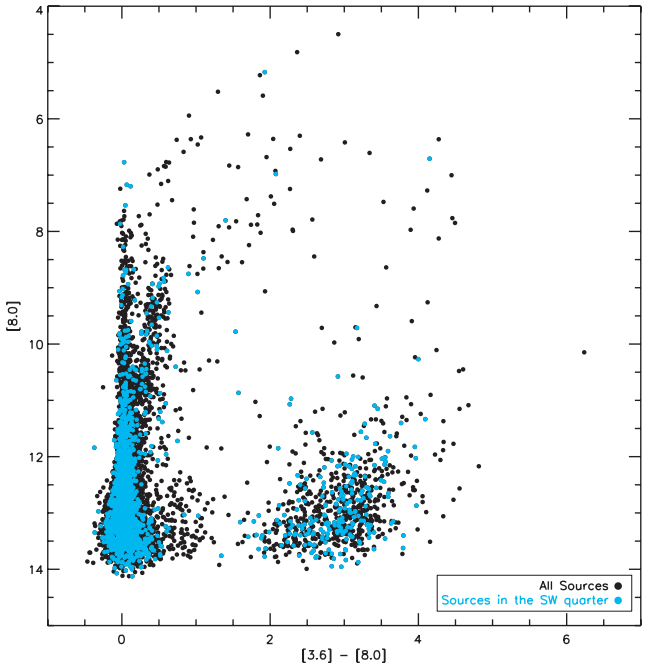

FIG. 13.—The [8.0] vs. [3.6] − [8] CMD for all sources detected in the N79/N83 region at these two wavelengths. Overplotted with cyan circles is the subset of sources in the southwest quarter of the N79/N83 region that is outside of the H II regions.

In contrast to the YSO population, the stars without dust and dusty evolved stars have a fair amount of structure in the CMDs. These two populations are well separated in the [8.0] versus $[K_s]$ − [8.0] and [8.0] versus [3.6] − [8.0] CMDs. The dusty evolved stars make two spurs to the brighter, redder part of the CMDs. This trend is seen most clearly in the [8.0] versus $[K_s]$ − [8.0] but is also present in the [4.5] versus [3.6] − [4.5] and [8.0] versus [3.6] − [8.0] CMDs. The stars without dust have a structure similar to that of the dusty evolved stars and appear as blue ends to these spurs that link the spurs to the column of stars at zero color. These sequences of dusty evolved stars are brighter than the [8.0] = 11 mag limit, above which dusty mass loss becomes important. The fact that the two spurs are separated in brightness may indicate two different populations that are separated in mass. The brighter of the two spurs probably represents the dusty RSGs, while the fainter spur is most likely the dusty AGB stars (see Fig. 2). Indeed, a number of the stars in the brighter spur have supergiant identifications from the survey of Westerlund et al. (1981). These brighter sources also appear variously in the CCD photometry catalog of Massey (2002), the *MSX* mid-IR catalog of Egan et al. (2001), and the study of luminous AGB stars by van Loon et al. (2005). These brightest red stars are also only present in the H II regions, as shown by the comparison of the CMDs for the whole N79/N83 region and those for a subset of this region that does not include the star formation regions (Figs. 13 and

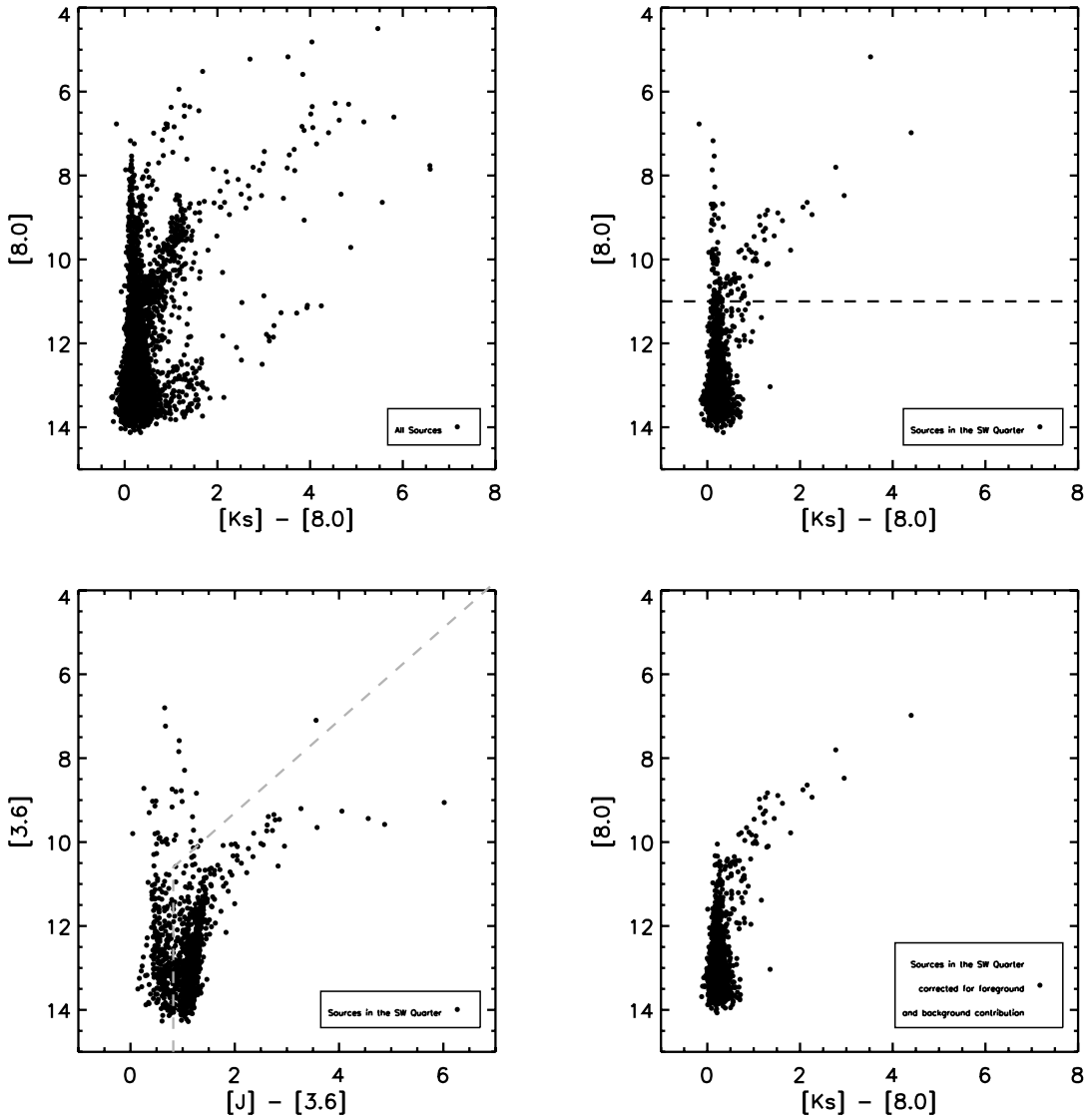

FIG. 14.—Near-IR (2MASS) and IRAC CMDs for sources detected in all seven bands in the N79/N83 region (*top left*). The southwest region (*top right*) contains sources detected in the N79/N83 southwest quarter and has been corrected for background galaxies based on the cuts of Fig. 11; see text. The [3.6] vs. $J - [3.6]$ diagram (*bottom left*) is effective in discriminating between foreground MW objects and LMC giants and AGB stars that should generally lie below and to the right of the dashed line (see text). The "corrected southwest" diagram (*bottom right*) shows the remaining sources, primarily LMC AGB stars, after removing foreground MW stars and background galaxy contributions. [*See the electronic edition of the Journal for a color version of this figure.*]

14). This association with ionized regions suggests that the stars of the brighter red spur are massive. A more detailed classification of these dusty evolved star populations will be discussed in a forthcoming paper by Blum et al. (2006).

4.4. *Background Galaxies and Foreground Milky Way Contributions*

The analysis of the SAGE survey requires an understanding of the MW foreground stellar contribution, as well as the background extragalactic component. Although we will make better estimates of the non-LMC contributions to the catalog when some off-LMC fields are analyzed, we develop some tools here to guide this effort and derive some preliminary numbers for these contributions to the point-source catalogs. Figures 13 and 14 show IRAC and 2MASS CMDs of the N79/N83 region and of the southwest quarter of this field. This southwest quarter contains all sources within a $0.^{\circ}41$ radius circle centered on and encompassing the southwest quarter of the N79/N83 region; and because it lies off the star formation regions, it should contain mostly older field stars in the LMC plus contributions from the foreground MW stars and background galaxies. The southwest region has 1576 sources detected in [3.6] and [8.0] in comparison to the 7595 sources in the N79/N83 region.

4.4.1. *Background Galaxies*

Figure 13 shows the [8.0] versus [3.6] − [8.0] CMD for all sources (*black*) that have been detected at these two wavelengths in the N79/N83 region. The cyan circles show just the subset of sources toward the southwest quarter of the region. This subset will naturally exclude stars and YSOs from the star-forming clusters but include LMC stars, MW foreground stars, and background galaxies. The LMC stars and MW foreground stars should populate the stars without dust and dusty evolved star regions of the CMD. We note that there is a large population of faint red sources in the YSO candidate region of the CMD in this off position (*cyan circles*), and here we discuss the possibility that all of these faint YSO candidates are background galaxies. Background galaxies in this region of the CMD have been a known

contaminant for the *Spitzer* Legacy program Cores to Disks (Evans 2003).

Fazio et al. (2004) have estimated the IRAC 8 μm galaxy counts in several northern fields. For two fields studied, Fazio et al. (2004) report approximately 900 galaxies per square degree at 8 μm for $[8.0] < 14.0$ mag, which is at our sensitivity limit (Table 2) for the present epoch 1 point-source catalog. In Figure 13 we count 219 sources with $[3.6] - [8.0] > 1$ mag and $14.0 > [8.0] > 10$ mag, i.e., the YSO region, in the southwest quarter, which would correspond to 425 galaxies per square degree at 8 μm. This good agreement between the faint YSO candidates with the galaxy counts of Fazio et al. (2004) suggests that most of these faint-candidate YSOs are background galaxies. This statistical estimation will not uniquely identify background versus LMC objects in young star-forming regions. The "Taurus" point shown in Figure 2 overlaps with the background galaxy region. However, most of the objects with $[3.6] - [8.0] > 1$ mag and $[8.0] > 10$ mag in the full survey region (*black points*) are likely to be galaxies. The percentage of such background galaxy candidates in the southwest quarter of the N79/N83 region is 14% of the total (=219/1576), scaling the number source density to the entire N79/N83 region suggests that 876 of the 7595 sources detected at 8 μm are background galaxies, or 12% of the total sample.

4.4.2. *Foreground Milky Way Stars*

Using 2MASS near-IR photometry in conjunction with the IRAC colors, we can similarly exclude MW foreground stars. In Figure 14 (*top left*), the [8.0] versus $K_s - [8.0]$ CMD is shown for all sources detected in the four IRAC bands plus J, H, and K in the 2MASS survey. The top right panel (southwest) of Figure 14 shows the same CMD, but only for sources in the southwest quarter of the N79/N83 region and excluding the background galaxies as described above ($[3.6] - [8.0] > 1$ mag and $[8.0] > 10$ mag). Most of the galaxies are already excluded by the requirement that each source be detected in J, H, and K and all four IRAC bands. The bulk of the objects lie along a vertical sequence near $K_s - [8.0] = 0$. These are a mixture of LMC giants and MW dwarfs and giants. A cursory check of the SIMBAD database for the bright objects near $K_s - [8.0] = 0$ and with $[8.0] < 7$ mag shows a number of HD stars with giant or dwarf classifications.

Foreground MW stars may be further distinguished from LMC stars by considering the [3.6] versus $J - [3.6]$ CMD as plotted in Figure 14 (*bottom left*; also restricted to objects in the southwest part of the N79/N83 field). These two colors span the largest wavelength baseline of the N79/N83 field photometry (IRAC and 2MASS) for which the stellar photosphere should be most important. The cool LMC giants and AGB stars are seen to extend to redder colors (roughly $J - [3.6] > 0.75$) compared to the bluer foreground objects and to fainter magnitudes (approximately $[3.6] > 10$ mag). For brighter [3.6], MW giants are redder; a K0 giant has $K - L = 0.75$ (Koornneef 1983). Making cuts in color and magnitude represented by stars below and to the right of the dashed line in Figure 14 (*bottom left*), the bulk of the southwest stars are LMC AGB stars, 997 of the 1296 objects included in the southwest diagram in Figure 14. The remaining stars are most likely foreground MW stars, which number 293 in total, or 23% of this southwest region sample, or 320 foreground MW stars per square degree in the field. Over the whole N79/N83 region, where the LMC source density is higher, the fraction of foreground MW stars is 18%.

Figure 14 (*bottom right*) shows the southwest region of the survey again but with the foreground stars from the [3.6] panel removed as described in the last paragraph. The mass-losing stars on the AGB extend to redder and brighter magnitudes in this panel.

5. SUMMARY

SAGE is an $\sim$500 hr *Spitzer* MIPS and IRAC imaging survey of a $\sim 7^\circ \times 7^\circ$ field of the LMC (Figs. 3 and 4) with characteristics summarized in Table 1. The SAGE data are nonproprietary, and the SAGE team is committed to delivering point-source lists and improved images to the SSC for community access in support of proposal cycles 4 and 5 of *Spitzer*. The science drivers for the survey center on the life cycle of baryonic matter in the LMC as traced by dust emission and, in particular, focus on the ISM, star formation, and evolved stars. We present initial results on the epoch 1 SAGE data for a region near N79 and N83 that provide a verification of the survey's goals and a start at interpreting the results. The measured point-source sensitivity for epoch 1 data is consistent with expectations for the SAGE survey. For the epoch 1 catalogs, we find 3.94×10^6 sources detected in the IRAC 3.6 μm band. The images and point-source counts show a similar trend. The stars dominate the light at the shortest wavelength of 3.6 μm, and the diffuse dust emission becomes increasingly important at the longer wavelengths and dominates in the MIPS 24, 70, and 160 μm images. The dust emission revealed by the combined MIPS 24, 70, and 160 μm bands and the IRAC 8.0 μm band traces all three phases of the ISM gas; however, the relative intensity of these dust emission bands varies with the ISM environment. Using MW templates as a guide, we adopt a simplified point-source classification to identify three candidate groups—stars without dust, dusty evolved stars, and YSOs—on the $[3.6] - [8.0]$ versus $[8.0] - [24]$ color-color diagram. This source classification scheme holds up well when sources are displayed in other color-color diagrams and CMDs for the LMC and offers a good starting point for follow-up work. When plotted on CMDs, the stars without dust and dusty evolved stars separate into main-sequence stars (with zero color), supergiants, and AGB stars. We develop a strategy for identifying the contribution to the SAGE point-source catalog of background galaxies, 155 deg^{-2} or $\sim$12% of sources in the N79/N83 region, and foreground MW stars, 320 deg^{-2} or $\sim$18% of sources in the N79/N83 region.

We are grateful to Bill Mahoney, Nancy Silberman, and Lisa Storrie-Lombardi and the staff at the *Spitzer* Science Center for their support in implementing the SAGE observing campaigns on *Spitzer*. Albeto Conti and Bernie Shiao of the Space Telescope Science Institute (STScI) were instrumental in setting up the SAGE database from which these results were extracted. We acknowledge useful discussions with Elena Sabbi. Zolt Levay of STScI created several of the color figures in this paper. This research has been funded by NASA *Spitzer* grant 1275598 and NASA grant NAG5-12595.

REFERENCES

Alard, C., et al. 2001, ApJ, 552, 289
Bakes, E., & Tielens, A. G. G. M. 1994, ApJ, 427, 822
Bekki, K., & Chiba, M. 2005, MNRAS, 356, 680
Benjamin, R. A., et al. 2003, PASP, 115, 953
Blitz, L., Fukui, Y., Kawamura, A., Leroy, A., Mizuno, N., & Rosolowsky, E. 2006, in Protostars and Planets V, ed. B. Reipurth, D. Jewitt, & K. Keil (Tucson: Univ. Arizona Press), in press (astro-ph/0602600)
Blum, R. D., et al. 2006, AJ, 132, 2034

Chu, Y.-H., et al. 2005, ApJ, 634, L189
Cioni, M.-R., et al. 2000, A&AS, 144, 235
Cohen, M. 1993, AJ, 105, 1860
Cohen, M., Staveley-Smith, L., & Green, A. 2003, MNRAS, 340, 275
Dale, D. A., Bendo, G. J., & Engelbracht, C. W. 2005, ApJ, 633, 857
Desert, F.-X., Boulanger, F., & Puget, J. L. 1990, A&A, 237, 215
Diolaiti, E., Bendinelli, O., Bonaccini, D., Close, L., Currie, D., & Parmeggiani, G. 2000, A&AS, 147, 335
Efremov, Y. N., & Elmegreen, B. G. 1998, MNRAS, 299, 643
Egan, M. P., van Dyk, S. D., & Price, S. D. 2001, AJ, 122, 1844
Engelbracht, C. W., Gordon, K. D., Rieke, G. H., Werner, M. W., Dale, D. A., & Latter, W. B. 2005, ApJ, 628, L29
Engelbracht, C. W., et al. 2006, ApJ, 642, L127
Evans, N. J. 2003, PASP, 115, 965
Fazio, G. G., et al. 2004, ApJS, 154, 39
Feast, M. 1999, in IAU Symp. 190, New Views of the Magellanic Clouds, ed. Y.-H. Chu et al. (San Francisco: ASP), 542
Fukui, Y., Mizuno, N., Yamaguchi, R., Mizuno, A., & Onishi, T. 2001, PASJ, 53, L41
Fukui, Y., et al. 1999, PASJ, 51, 745
Galliano, F., Madden, S. C., Jones, A. P., Wilson, C. D., & Bernard, J.-P. 2005, A&A, 434, 867
Gatley, I., Hyland, A. R., & Jones, T. J.1982, MNRAS, 200, 521
Gaustad, J. E., McCullough, P. R., Rosing, W., & Van Buren, D. 2001, PASP, 113, 1326
Glass, I. S., et al. 1999, MNRAS, 308, 127
Gordon, K. D., Clayton, G. C., Misselt, K. A., Landolt, A. U., & Wolff, M. J. 2003, ApJ, 594, 279
Gordon, K. D., et al. 2004, ApJS, 154, 215
———. 2005, PASP, 117, 503
Gorjian, V., et al. 2004, ApJS, 154, 275
Harris, J., & Zaritsky, D. 2004, AJ, 127, 1531
Heydari-Malayeri, M., Charmandaris, V., Deharveng, L., Rosa, M. R., Schaerer, D., & Zinnecker, H. 2001, A&A, 372, 495
Holtzman, J., et al. 1999, AJ, 118, 2262
Hora, J. L., et al. 2004, Proc. SPIE, 5487, 77
Houck, J. R., et al. 2004, ApJS, 154, 211
Israel, F. P., et al. 2003, A&A, 406, 817
Jones, T. J., Woodward, C. E., Boyer, M. L., Gehrz, R. D., & Polomski, E. 2005, ApJ, 620, 731
Kim, S., Staveley-Smith, L., Dopita, M. A., Sault, R. J., Freeman, K. C., Lee, Y., & Chu, Y.-H. 2003, ApJS, 148, 473
Koornneef, J. 1983, A&A, 128, 84
Loup, C., Zijlstra, A. A., Waters, L. B. F. M., & Groenewegen, M. A. T. 1997, A&AS, 125, 419
Loup, C., et al. 1999, in IAU Symp. 191, Asymptotic Giant Branch Stars, ed. T. Le Bertre, A. Lebre, & C. Waelkens (San Francisco: ASP), 561
Madau, P., Ferguson, H. C., Dickinson, M. E., Giavalisco, M., Steidel, C. C., & Fruchter, A. 1996, MNRAS, 283, 1388
Madden, S. C. 2000, NewA Rev., 44, 249
Madden, S. C., Galliano, F., Jones, A. P., & Sauvage, M. 2006, A&A, 446, 877
Massey, P. 2002, ApJS, 141, 81
Mizuno, N., et al. 2001, PASJ, 53, 971
Nikolaev, S., & Weinberg, M. D. 2000, ApJ, 542, 804
Oey, S., & Massey, P. 1995, ApJ, 452, 210
O'Halloran, B., Satyapal, S., & Dudik, R. P. 2006, ApJ, 641, 795
Olsen, K. A. G. 1999, AJ, 117, 2244
Panagia, N., Romaniello, M., Scuderi, S., & Kirshner, R. P. 2000, ApJ, 539, 197
Pei, Y. C., Fall, S. M., & Hauser, M. G. 1999, ApJ, 522, 604
Ramdani, A., & Jorissen, A. 2001, A&A, 372, 85
Reach, W. T., et al. 2005, PASP, 117, 978
Schwering, P. B. W. 1989, A&AS, 79, 105
Smith, A. W., Cornett, R. H., & Hill, R. S. 1987, ApJ, 320, 609
Staveley-Smith, L., Kim, S., Calabretta, M. R., Haynes, R. F., & Kesteven, M. J. 2003, MNRAS, 339, 87
Stetson, P. 1987, PASP, 99, 191
Tielens, A. G. G. M. 2001, in ASP Conf. Ser. 231, Tetons 4: Galactic Structure, Stars, and the Interstellar Medium, ed. C. E. Woodward, M. D. Bicay, & J. M. Shull (San Francisco: ASP), 92
Trams, N. R., et al. 1999, A&A, 346, 834
van der Marel, R., & Cioni, M.-R. L. 2001, AJ, 122, 1807
Van Dyk, S. D., Cutri, R., Weinberg, M. D., Nikolaev, S., & Sktutskie, M. F. 1999, in IAU Symp. 190, New Views of the Magellanic Clouds, ed. Y.-H. Chu et al. (San Francisco: ASP), 363
van Loon, J. T., Groenewegen, M. A. T., de Koter, A., Trams, N. R., Waters, L. B. F. M., Zijlstra, A. A., Whitelock, P. A., & Loup, C. 1999, A&A, 351, 559
van Loon, J. T., Marshall, J. R., & Zijlstra, A. A. 2005, A&A, 442, 597
Vermeij, R., & van der Hulst, J. M. 2002, A&A, 391, 1081
Walborn, N. R., Barba, R. H., Brandner, W., Rubio, M., Grebel, E. K., & Probst, R. G. 1999, AJ, 117, 225
Werner, M., et al. 2004, ApJS, 154, 1
Westerlund, B. E. 1997, The Magellanic Clouds (New York: Cambridge Univ. Press)
Westerlund, B. E., Olander, N., & Hedin, B. 1981, A&AS, 43, 267
Whitney, B., Indebetouw, R., Bjorkman, J. E., & Wood, K. 2004, ApJ, 617, 1177
Willner, S. P., et al. 2004, ApJS, 154, 222
Wolfire, M., Hollenbach, D., McKee, C. F., Tielens, A. G. G. M., & Bakes, E. L. O. 1995, ApJ, 443, 152
Wood, P. R., et al. 1999, in IAU Symp. 191, Asymptotic Giant Branch Stars, ed. T. Le Bertre, A. Lebre, & C. Waelkens (San Francisco: ASP), 151
Wu, Y., Charmandaris, V., Hao, L., Brandl, B. R., Bernard-Salas, J., Spoon, H. W. W., & Houck, J. R. 2006, ApJ, 639, 157
Yamaguchi, R., et al. 2001, PASJ, 53, 985
Zaritsky, D., & Harris, J. 2004, ApJ, 604, 167
Zaritsky, D., Harris, J., Thompson, I. B., & Grebel, E. K. 2004, AJ, 128, 1606